Neuntrino opportunities at Jinping

Jinping neutrino program working group*

Working edition produced on May 28, 2015

Abstract

Jinping underground lab with an extremely low cosmic-ray muon flux and a low reactor neutrino flux is an ideal site to do low background experiments. In this note, we estimated the potential to do neutrino physics research at Jinping, which includes solar neutrino physics, supernova relic and burst neutrinos search, geoneutrinos, atmosphere neutrinos, and neutrinos from dark matter annihilations. Some preliminary conclusion about the fiducial detector volume (>1 kilo-ton) and technology (water-based liquid scintillator, etc.) are made. More detailed studies are in progress.

Contents

*Questions and comments can be sent to chenshaomin@tsinghua.edu.cn and wangzhe-hep@tsinghua.edu.cn.

1 Experimental site

1.1 Overview

China JinPing underground Laboratory (CJPL) [1] is one of ideal sites to do low background experiments in the world. The experimental site is located in Jinping Mountain, Sichuan Province, China (Fig. 1). Jinping Mountain measures 4,100-4,500 meters high and is surrounded by Yalong River. A 150-km river bend surrounds the mountain with a water level difference of 312 m between both sides. China Yalong River Hydropower Development Company (Yalong Hydro, previously known as Ertan Hydropower Development Company) has built the Jinping II Hydropower Station, including four headrace tunnels, two traffic tunnels and one drainage tunnel across the Jinping Mountain (Fig. 2). The headrace tunnels are about 16.7 km in length and 12.4-13.0 m in diameter, with a maximum overburden of 2375 m (6650 meter water equivalent assuming a constant rock density 2.8 g/cm^3). More than 75% of the tunnel depth is larger than 1700 m. Two traffic tunnels are parallel to the headrace tunnels: #A (5 m in width and 5.5 m in height) and #B (6 m in width and 6.5 m in height). The drainage tunnel with a diameter of 7.2 m is located between traffic tunnel #B and headrace tunnel #4. All seven tunnels were finished in August 2008 and are all now maintained by Yalong Hydro.

Figure 1: (Color online) China JinPing underground Laboratory (CJPL) is located in Jinping Mountain, Sichuan Province, China. Jinping Mountain is surrounded by Yalong River as the solid blue line in the right plot, and the position of Jinping tunnels is indicated by the dashed line. The distance to the closest airport is about 2 hours' drive.

The first phase of Jinping laboratory was constructed in the middle of the traffic tunnels at the end of 2009. The lab was used for two dark matter experiments: CDEX [2] and PandaX [3]. The second phase of Jinping laboratory started in the end of 2014. The construction plan is to build four 150 m long tunnels not far away from the traffic tunnels as shown in Fig. 2.

This plan is to use one of the new tunnels to build a neutrino experiment with fiducial mass at kiloton scale. The initial plan is to adopt water Cherenkov technique as the base line design, with a capacity of extension to water-based scintillator and even scintillator detector.

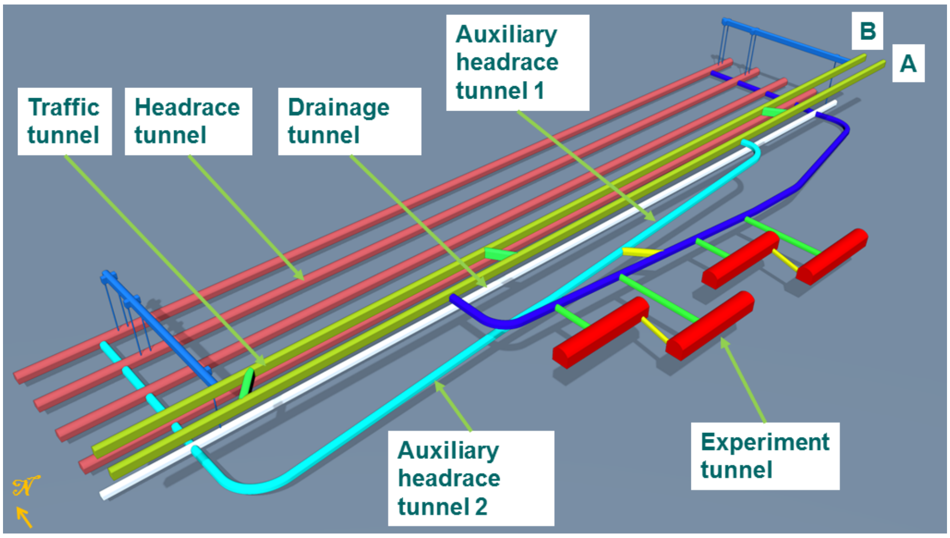

Figure 2: (Color online) Schematic of Jinping tunnels and Jinping phase II laboratories.

1.2 Geological conditions and geotechnical feasibility

The Yalong River is located in the geomorphological level II ladder of the transition zone from the Tibetan Plateau to the Sichuan Basin. The altitude decreases from about 5000 m in the northwest to approximately 2000 m in the southeast. The Jinping Mountain extends along a nearly N-S direction. Many of the peaks are higher than 3000 m in altitude, with a maximum relative elevation difference of 3150 m. The main watershed lies along an N-S axis and is slightly oriented to the west. The regional distribution of mountain is basically consistent with the tectonic line. Generally the topography of the Jinping laboratory region appears as undulating ground surface and has large differences in elevation (Fig. 3).

1.2.1 In-situ stress

The complicated mountainous topography, lithologies, geological structures (faulting and folding, and a complex geological history) directly lead to a sophisticated stress field in the Jinping Mountain (Fig. 4). At the both ends of the tunnels near the river valley, horizontal stresses are larger than the vertical stress, and a TF-type (Thrust faulting) of stress regime is expected with the sequence of $\sigma_H > \sigma_h > \sigma_v$, where σ_H is the maximum horizontal stress, σ_h is the minimum horizontal stress, and σ_v is the vertical stress. The Jinping laboratory site has an overburden of about 2450 m, and the vertical stress is up to about 66 MPa, which is dominated by gravity stress. The maximum and minimum horizontal in-situ stresses are about 55 MPa and 44 MPa, respectively. The principal stress regime is NF (Normal faulting) with the sequence of $\sigma_v > \sigma_H > \sigma_h$. There might be a regime transition zone between the stress field near the river valley and that at the maximum buried depth, where the stress sequence would be $\sigma_H > \sigma_v > \sigma_h$ corresponding to SS (Strike-slip faulting) stress regime.

1.2.2 Hydrological conditions

The distribution of fractured and karst groundwater is complex due to local variations in hydrogeological conditions. At the eastern and western ends of the Jinping tunnels, karst geology structures were exposed by excavation, and karst water was predominant groundwater at both ends. However,

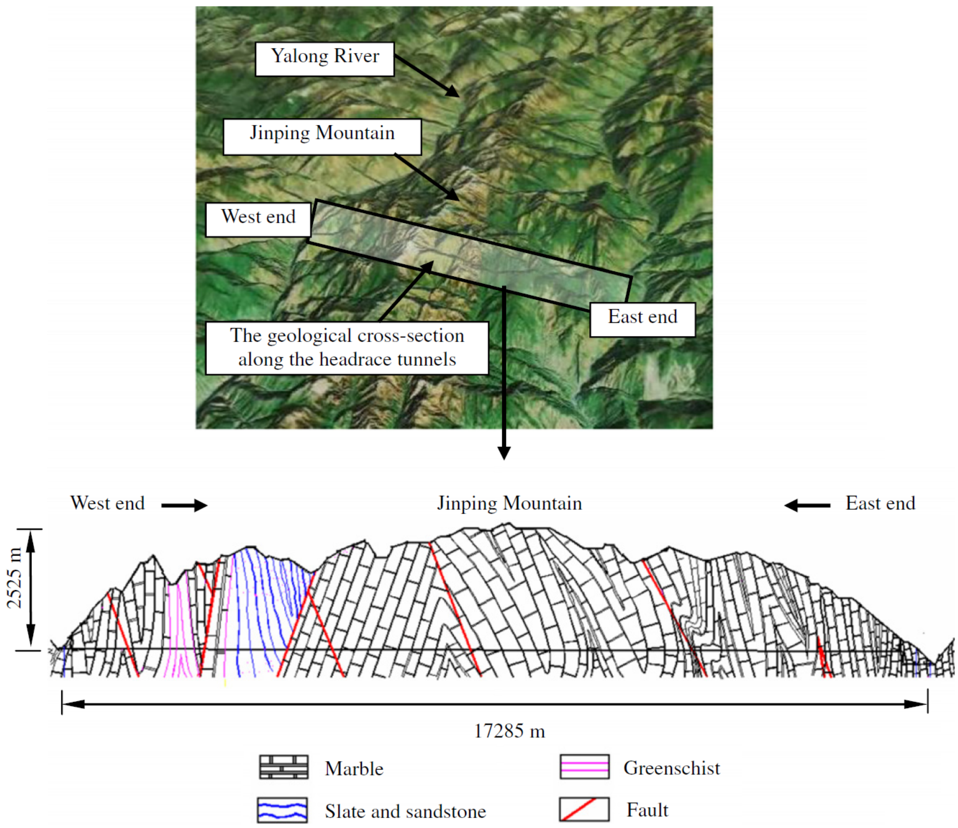

Figure 3: (Color online) Geological cross-section along the headrace tunnels of the Jinping II Hydropower Station [4].

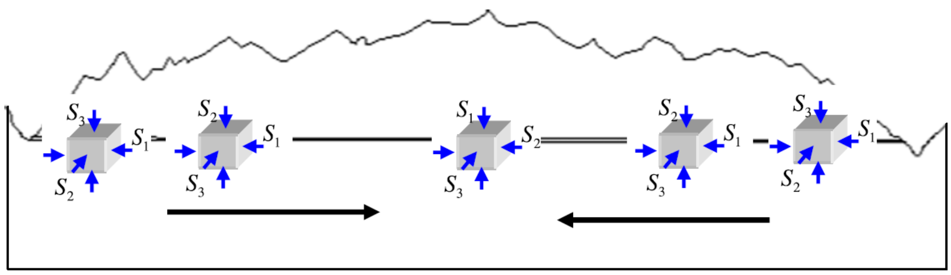

Figure 4: (Color online) Prediction of the macro-distribution of in-situ stress along the headrace tunnels of the Jinping II Hydropower Station [4]. The stress magnitudes are defined using the standard geologic/geophysical notation with S1>S2>S3, where S1 is the maximum principal stress, S2 is the intermediate principal stress, and S3 the minimum principal stress.

in the middle of the tunnels and the experimental site under the large overburden, the groundwater distribution is inhomogeneous and probably concentrated on local tunnel regions, where rapid water influx may occur. The groundwater includes both fractured and karst water. Seven heavy water in-rush events were recorded during the excavation of the two traffic tunnels. Their water pressures ranged from 0.6 to 4.7 MPa and their influx flow rates ranged from 0.15 to 15.6 m^3/s [5].

1.2.3 Main rock mechanical parameters

Along the Jinping tunnels, harder rocks (i.e. marble and sandstone) and softer rocks (i.e. chlorite schist and sand slate) compose the feature of rock mass, and marble is the main rock in the engineering region of Jinping Laboratory. The unconfined compressive strength (UCS) of Jinping marble is between 95 and 105 MPa, and its damage initiation stress is between 40 and 50 MPa.

1.2.4 Excavation damage zone

Under high stress condition, the conflict between the strength of rock mass and the stress can lead to damage in the vicinity of the experimental hall. Acoustic testing and borehole television were used to monitor the size of the damage zone around Jinping headrace tunnel #4, and the results showed that the damage zone appears an asymmetric shape, i.e. the depth of the north side of the headrace tunnel #4 was much larger than that of the south side (Fig. 5).

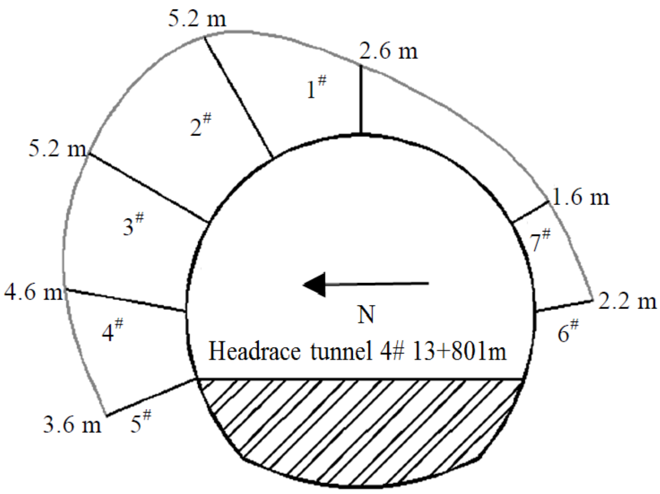

Figure 5: Excavation damage zone of Section 13+801m of Jinping headrace tunnel #4 [6].

1.2.5 Risks of rock bursts

Rock-bursts were observed in the massive marble in the Jinping tunnels from approximately 1700 m of overburden. More than 100 rock-burst events, of varying extents and severities, occurred during the excavation of the four headrace tunnels and the drainage tunnel with depth larger than 1900 m. Among them, a severe rock-burst event occurred on 28 November, 2009 during TBM tunnelling in the drainage tunnel. Due to the instant impact of this rock-shock, all support systems were destroyed, the main beam of the TBM equipment was broken, and a space of about 30 m behind the cutter head was buried in debris. Seismic events, both before and during the rock-burst, were recorded using micro-seismic monitoring equipment, which indicated a Richter magnitude of 2.0.

1.2.6 Future studied needed

Overall, to host a large experimental hall for a kiloton scale neutrino detector, a couple of geotechnical challenges still exist, e.g., rock bursts, water influx, and large deformation. During the conceptual design phase, the conclusions to the following issues will be given (1) Experimental hall

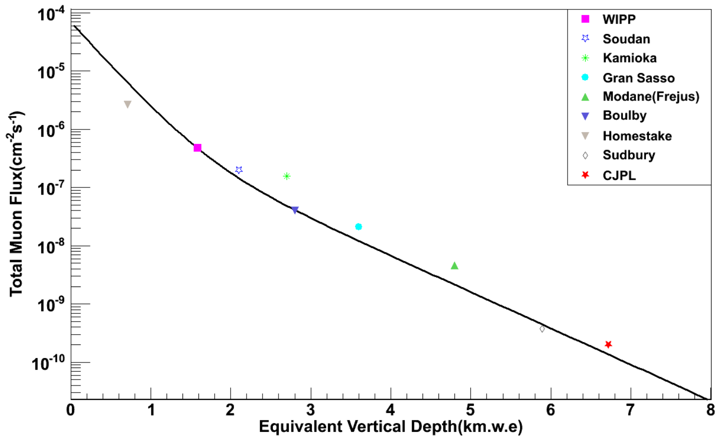

Figure 6: (Color online) Cosmic-ray muon flux of CJPL and a comparison with other laboratories.

layout, (2) Excavation and support method, (3) Water Supply and Drainage, (4) Electricity and Ventilation System, and (5) Risks during construction and operation.

1.3 Cosmic-ray muon flux

Cosmic-ray muon itself can be easily detected and vetoed, but muon induced spallation backgrounds, especially fast neutrons and long lifetime isotopes are extremely dangerous for low background counting experiments. The rejection method usually includes a large buffer region to tag original muons and a long veto time window, which consumes a lot of space and detection efficiency. However cosmic-ray muon flux decreases sharply when the depth is getting larger. According to an in-situ measurement [7], the muon flux is as low as $(2.0 \pm 0.4) \times 10^{-10}/(\mathrm{cm}^2 \cdot \mathrm{s})$. A comparison with other underground labs can be seen in Fig. 6.

1.4 Reactor neutrino background

Jinping is also far away from all current running and being constructed nuclear power plants [8]. A world map with all nuclear power plants and SNO, Gran Sasso, Kamland and Jinping laboratories is shown in Fig. 7. The reactor electron antineutrino background is rather low and will be explained in later sections.

References

[1] K. J. Kang *et al.*, Journal of Physics: Conference Series **203**, 012028 (2010).

[2] Q. Yue *et al.*, Phys. Rev. **D90**, 091701 (R) (2014).

[3] M. J. Xiao *et al.*, Sci China-Phys Mech Astron, **57**, 2024 (2014).

[4] C. Zhang *et al.*, Int. J. Rock Mech. Min. Sci. **52**, 139 (2012).

[5] X. T. Feng *et al.*, 8th Asian Rock Mech. Sym. (2014).

[6] N. Liu *et al.*, Chin. J. Rock Mech. Eng. 32, 2235 (2013).

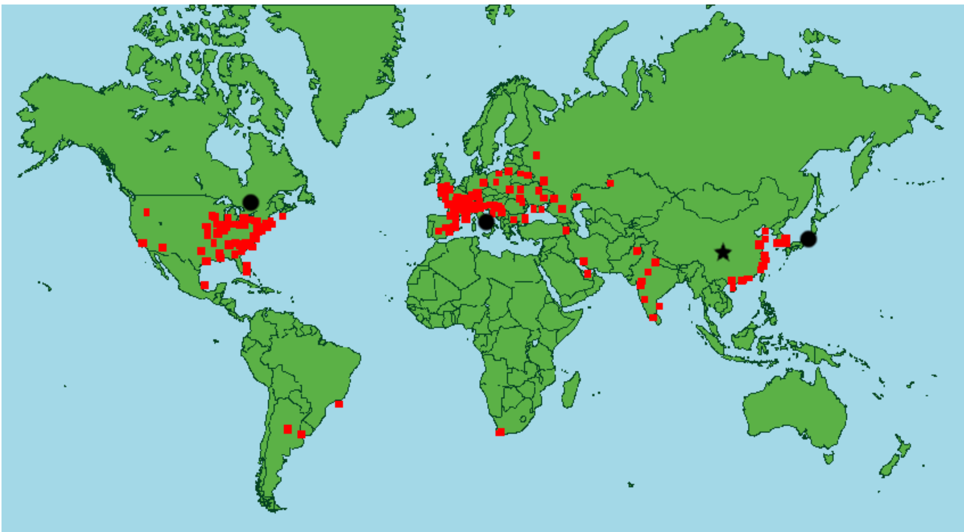

Figure 7: (Color online) World map with all currently running and being constructed nuclear power plants and SNO, Gran Sasso, Kamland and Jinping laboratory locations marked.

[7] Y. C. WU, Chinese Phys. **C37**, 086001 (2013).

[8] International Atomic Energy Agency, http://www.iaea.org/ (2015).

2 Solar neutrino

Particles from the external space are of great interest to people. Neutrinos, as a stellar probe, are featured by their extremely low interaction cross sections, which are not comparable by gammas, optical photons and protons. Neutrinos can easily reach our detectors without being interrupted by matters on their path. The original status, i.e. energy and direction, is maximally maintained, except that the flavor will oscillate, and consequently more information about the initial interaction can be probed. In principle, several kinds of astrophysical or cosmological neutrinos should exist, for example, supernova burst neutrinos, supernova relic neutrinos, Big Bang relic neutrinos, solar neutrinos. The Sun is the only well known and experimentally established astrophysical neutrino source. The knowledge of the Sun is critical to further understand the stars at distant space. The study of solar neutrinos can help to reveal the internal structure of the Sun, which can be complementary to optical observations. It is also helpful to draw a complete picture about neutrino physics, that won't be accomplished solely by terrestrial experiments. The technique to detect solar neutrino is now entering into a mature stage. Compared with the scale of modern high energy experiments, a relatively compact detector can still be constructed to pursue a precise measurement of the solar neutrinos.

Solar models, neutrino theories, and solar neutrino experiments have a rapid development in the past half a century, and the remarkable history has been described in [1, 2, 3, 4] and references therein. Nowadays the Sun is described by the Standard Solar Model (SSM) [5]. The Sun fuels itself by pp and CNO fusion processes. The evolution of the Sun relies on the radiation transparency, the convective motion, and the balance of gravity and radiative and particle pressure. The whole process is constrained by several boundary conditions: initial abundances of H, He, and other metal isotopes, current solar optical luminosity, mass, radius, etc. The SSM describes the whole life of the Sun from its pre main-sequence time to the current day, even to the future. The first solar neutrino flux measurement result, dominantly for ν_e component detected using ^{37}Cl as a detector, at Homestake [6] is 30% of the prediction, which indicates the major triumph of the SSM. The following steady experimental effort by SAGE(^{71}Ga detector) [7], GALLEX(^{71}Ga detector) [8], GNO [9], Kamiokande(water Cherenkov detector) [10], and Super Kamiokande(water Cherenkov detector) [11] all confirmed this measurement. Later SNO [12] experiment used a heavy water detector to make a measurement sensitive to all flavors, whose result agrees with the SSM prediction. Today we understand that electron neutrinos, ν_e, generated through the fusion processes inside the Sun may oscillate to other flavors [13, 14], ν_μ or ν_τ, and this behavior is further affected by the dense surrounding materials in the Sun, also known as matter, MSW, effect [15, 16]. These solar neutrino measurement results are the major trigger to study neutrino oscillation theory and carry out other atmosphere, reactor and accelerator neutrinos experiments.

Recently Borexino [17] experiment identified separately low energy ^7Be, pep and pp neutrinos as predicted by the SSM and the measured fluxes agree within their uncertainties with the SSM with MSW effect considered. But there are still questions to answer about the property of neutrinos and the solar model [18, 19, 20],

- Discovery of the missing solar neutrino components and improvement on the precisions of the known fluxes [21, 22, 2]. The search of CNO neutrinos is important on its own. The CNO neutrinos, which are minor in fraction of solar neutrinos, however dominate the fueling process of high temperature stellars, have not yet observed directly by any neutrino experiment. Improving the precisions of other solar neutrino components will be able to provide a tighter constrain on the solar model and play a role in study the following oscillation problems.

- A full picture of MSW effect in solar electron neutrino oscillation. The oscillation of low energy

ν_e, < 1 MeV, is like happening in vacuum. In the high electron density environment of the core of the Sun, with the increasing of neutrino energy, the MSW effect becomes dominant, and the transition of ν_e to other flavors turns to maximum. However this transition from vacuum to matter is still poorly constrained by experiments [23, 24, 25].

- Neutrino ν_e regeneration in the Earth. The matter effect of the Earth continues to change the phases of all solar neutrino components when they went through at the Earth, which is another evidence of MSW. The solar electron neutrinos after passing the Earth in the night, have a higher flux than the day time flux [26, 27]. The best experiment significance is 2.7σ by Super Kamiokande [28].

- Metallicity problem. As discussed in [29, 30], an improved solar model prediction is available with the input of the most up-to-date photosphere abundance of metals, which is 30% lower than early results. The new calculation predicts lower fluxes for several neutrinos components. The new predictions, low metallicity, and the orignal ones, high metallicity, are in serious conflict. The next generation of solar neutrino experiments are expected to be in the sensitive range to explore these unknowns.

In this section, a simulation study was carried out under the context of the Jinping underground laboratory, and is described in detail in section 2.1. With a discussion about the possible systematics 2.1.9, several issues are investigated for the MSW effects and the solar model. The sensitivity to detect each solar neutrino component is shown in section 2.2. The potential to study the transition of vacuum-matter oscillation and day-night asymmetry are discussed in section 2.3 and 2.4, respectively. The sensitivity to distinguish high and low metallicity models is shown in section 2.5.

2.1 Overview of the simulation study

A simulation study is done with default settings at Jinping, including the expected signal and background levels, energy resolution, target mass, and live time, then followed by an analysis for each physics topic.

2.1.1 Solar neutrino model

The neutrino energy spectra for all solar neutrino components are taken from [5]. The average neutrino flux predictions on the Earth without oscillation are from [30] and [31] for high and low metallicity hypotheses, respectively. The spectra with high metallicity flux prediction are shown in Fig. 8 and all the values of fluxes are listed in table 1.

2.1.2 Oscillation probability

The propagation of solar neutrinos goes through three separate segments: 1) from the core of the Sun to its surface; 2) from the surface of the Sun to the surface of the Earth; 3) the path through the Earth if it is detected at night.

The survival probability of solar electron neutrinow with energy E_ν from the core of the Sun to its surface must include the matter effect [15, 16] and can be approximated by the following formula [19],

$$P_{ee}^{\odot} = \cos^4\theta_{13}(\frac{1}{2} + \frac{1}{2}\cos 2\theta_{12}^{M}\cos 2\theta_{12}), \tag{1}$$

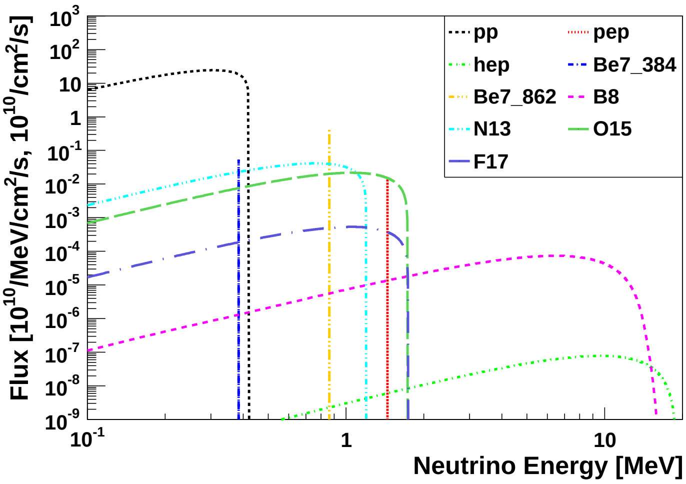

Figure 8: (Color online) Solar neutrino energy spectra and fluxes with the high metallicity hypotheses, where the unit for continuous spectra is 10^{10}/MeV/cm^2/s, and for discrete lines is 10^{10}/cm^2/s.

	E_{Max} or E_{Line} [MeV]	Flux (GS98) high metallicity [$\times 10^{10}$s^{-1}cm^{-2}]	Flux (AGS09) low metallicity [$\times 10^{10}$s^{-1}cm^{-2}]
pp	0.42 MeV	$5.98(1 \pm 0.006)$	$6.03(1 \pm 0.006)$
^{7}Be	0.38 MeV	$0.053(1 \pm 0.07)$	$0.048(1 \pm 0.07)$
	0.86 MeV	$0.447(1 \pm 0.07)$	$0.408(1 \pm 0.07)$
pep	1.45 MeV	$0.0144(1 \pm 0.012)$	$0.0147(1 \pm 0.012)$
^{13}N	1.19 MeV	$0.0296(1 \pm 0.14)$	$0.0217(1 \pm 0.14)$
^{15}O	1.73 MeV	$0.0223(1 \pm 0.15)$	$0.0156(1 \pm 0.15)$
^{17}F	1.74 MeV	$5.52 \times 10^{-4}(1 \pm 0.17)$	$3.40 \times 10^{-4}(1 \pm 0.17)$
^{8}B	15.8 MeV	$5.58 \times 10^{-4}(1 \pm 0.14)$	$4.59 \times 10^{-4}(1 \pm 0.14)$
hep	18.5 MeV	$8.04 \times 10^{-7}(1 \pm 0.30)$	$8.31 \times 10^{-7}(1 \pm 0.30)$

Table 1: Solar neutrino flux predictions without oscillation based on the high and low metallicity hypothesis [30, 31]. The production branching ratios of the 0.38 and 0.86 MeV ^{7}Be lines are 0.1052 and 0.8948, respectively.

where the mixing angle in matter is

$$\cos 2\theta_{12}^M = \frac{\cos 2\theta_{12} - \beta}{\sqrt{(\cos 2\theta_{12} - \beta)^2 + \sin^2 2\theta_{12}}}, \tag{2}$$

with

$$\beta = \frac{2\sqrt{2} G_F \cos^2\theta_{13} n_e E_\nu}{\Delta m^2_{12}}, \tag{3}$$

where G_F is the Fermi coupling constant and n_e is the density of electrons in the neutrino production place of the Sun. The calculation is under a good assumption of adiabatic evolution [32], so that the density of electrons varies slowly and does not causes any exchange among the mass eigenstates after being created. It is noted that for the solar case only the initial n_e for the neutrino production place is required. Using $\sin^2\theta_{12}$=0.307, $\sin^2\theta_{13}$=0.0241, $\Delta m^2_{12} = 7.54 \times 10^{-5}\ eV^2$, and solar center $n_e = 6 \times 10^{25}/cm^3$ [33], the survival probability is shown in Fig. 9. No consideration is taken for the generation radius distribution of each component. Correspondingly the appearance probability of ν_μ and ν_τ is

$$P^{\odot}_{e\mu(\tau)} = 1 - P^{\odot}_{ee}. \tag{4}$$

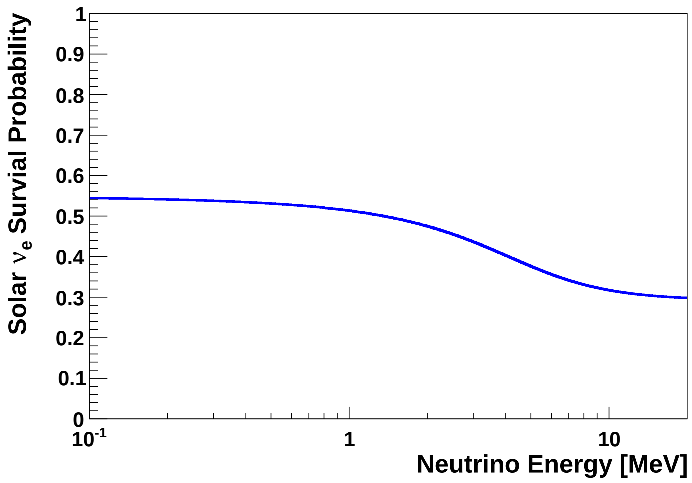

Figure 9: (Color online) Solar electron neutrino survival probability.

The second segment is the neutrino propagation from the surface of the Sun to the surface of the Earth. We consider that the mass eigenstates of neutrinos emerging from the surface of the Sun are decoherent [34] due to the sizable width of the energy spectrum of each neutrino component, even for ^{7}Be neutrinos [35]. The amplitudes of all mass eigenstates keep unchanged even reaching the surface of the Earth and are still decoherent. The fluxes only decrease by a factor of the Earth-Sun distance squared with a percent-level annual modulation effect due to the eccentric orbit of the Earth. Since the fluxes used are the predicted averages on the surface of the Earth without oscillation, the above oscillation probability $P_{ee}^{\odot}$ is sufficient for most of the studies.

To study the day-night asymmetry of solar neutrino flux, a full numerical calculation based on the three-generation oscillation is used [36]. We assume that both the adiabatic condition and the decoherent property are still valid. The probability of detecting a solar electron neutrino is

$$P_{ee} = \sum_{i=1,2,3} P_{ei}^{\odot} P_{ie}^{\oplus}, \tag{5}$$

where $P_{ei}^{\odot}$ is the probability of solar electron neutrinos surviving as their mass eigenstates ν_i ($i = 1, 2, 3$) on the surface of the Sun, and $P_{ie}^{\oplus}$ is the appearance probability of solar electron neutrino for each mass eigenstate ν_i when they pass through the Earth. The $P_{ei}^{\odot}$ is determined by the local n_e in the production place of the Sun ν_e. $P_{ie}^{\oplus}$ has to be calculated numerically through a multi-shell model of the Earth as explained below. The result for the day time is the same as eq. 1.

2.1.3 Earth shell model

Two different 6-shell models of the Earth [37, 38] are used. One density profile is for continental region, i.e. Jinping, which is all surrounded by rock, whose density is 3 g/cm^3, and the other one is for experiments close to ocean, i.e. Super-Kaminokande, which is surrounded by 8 km deep ocean, whose density is 1 g/cm^3 [39]. The two different models are shown in Fig. 10 and Fig. 11. n_e to the density ratio is set to 0.47 mol/cm^3 for inner shells and 0.50 mol/cm^3 for outer shells, respectively. As will be seen later, the ν_e regeneration in the Earth is only sensitive to the surface density and is not sensitive to the path length in the Earth.

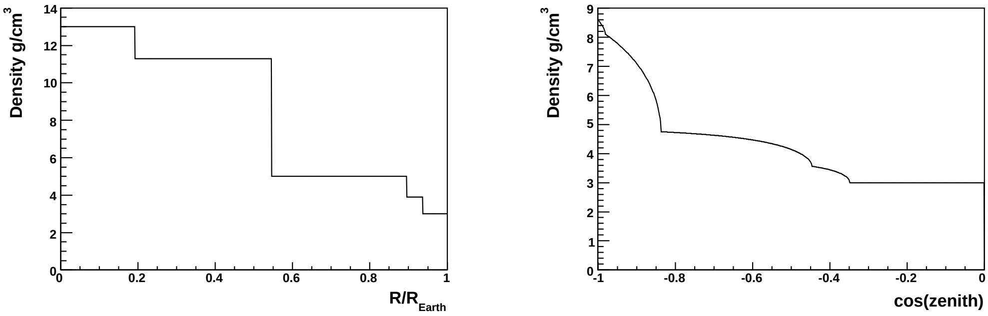

Figure 10: Density dependence of depth for continental experiments. Left is density vs. radius, and the right is average density vs. cosine of zenith angle.

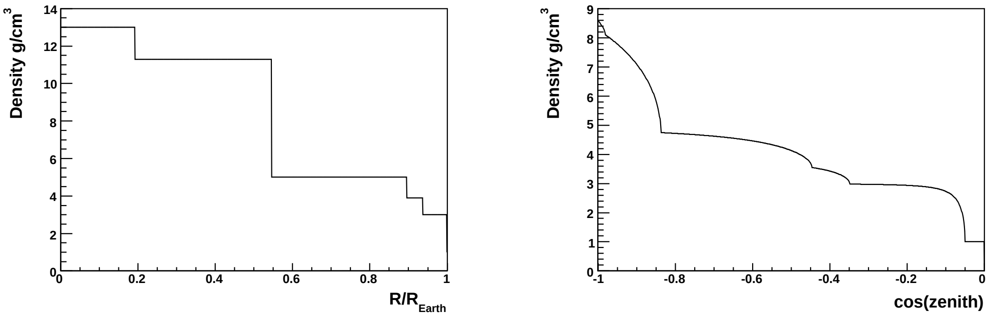

Figure 11: Density dependence of depth for experiments next to ocean. Left is density vs. radius, and the right is average density vs. cosine of zenith angle.

2.1.4 Elastic scattering cross section

The neutrino electron elastic scattering process will be used to detect solar neutrinos. The scattered electron's energy and direction can be measured and used to derive the incoming neutrino energy and direction. The differential scattering cross-sections as a function of the kinetic energy of the recoil electron, T_e, and neutrino energy, E_ν, in the electron rest frame can be written, for example, in [40] as:

$$\frac{d\sigma(E_\nu, T_e)}{dT_e} = \frac{\sigma_0}{m_e}\left[g_1^2 + g_2^2(1 - \frac{T_e}{E_\nu})^2 - g_1 g_2 \frac{m_e T_e}{E_\nu^2}\right], \tag{6}$$

with

$$\sigma_0 = \frac{2G_F^2 m_e^2}{\pi} \simeq 88.06 \times 10^{-46} cm^2, \tag{7}$$

where m_e is the electron mass. Depending on the flavor of the neutrino, g_1 and g_2 are:

$$\begin{aligned} g_1^{(\nu_e)} &= g_2^{(\bar{\nu}_e)} = \frac{1}{2} + \sin^2\theta_W \simeq 0.73, \\ g_2^{(\nu_e)} &= g_1^{(\bar{\nu}_e)} = \sin^2\theta_W \simeq 0.23, \end{aligned} \tag{8}$$

where θ_W is the Weinberg angle, then for $\nu_{\mu,\tau}$ they are

$$\begin{aligned} g_1^{(\nu_{\mu,\tau})} &= g_2^{(\bar{\nu}_{\mu,\tau})} = -\frac{1}{2} + \sin^2\theta_W \simeq -0.27, \\ g_2^{(\nu_{\mu,\tau})} &= g_1^{(\bar{\nu}_{\mu,\tau})} = \sin^2\theta_W \simeq 0.23. \end{aligned} \tag{9}$$

The total cross section, differential ν_e electron scattering cross section as a function of T_e and the cosine angle between recoiled electron and initial neutrino direction are shown in Fig. 12.

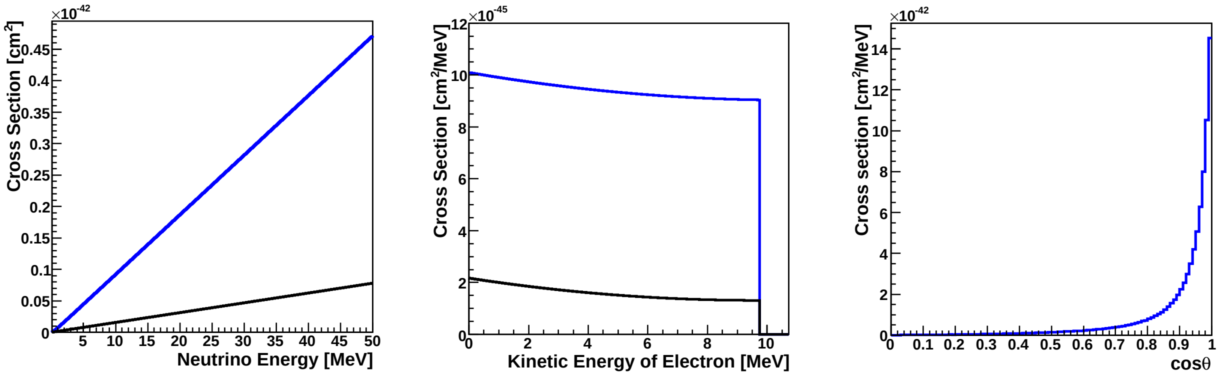

Figure 12: (Color online) From left to right are total ν_e, blue, ($\nu_{\mu,\tau}$, black) electron scattering cross section as a function of neutrino energy, differential scattering cross-section as a function of the kinetic energy of recoiled electron for a 10 MeV neutrino, and the distribution of the cosine angle between recoiled electron and initial neutrino direction for a 10 MeV ν_e.

2.1.5 Detectable electron spectrum

In fact, the observed electron kinetic energy spectrum contains all the contributions from electron-, muon- and tau-neutrinos. The electron kinetic energy spectrum can be expressed as:

$$R_\nu = N_e \Phi_\nu \int dE_\nu \frac{d\lambda}{dE_\nu} \int \left\{ \frac{d\sigma_e(E_\nu, T_e)}{dT_e} P_{ee}(E_\nu) + \frac{d\sigma_{\mu,\tau}(E_\nu, T_e)}{dT_e} \left[1 - P_{ee}(E_\nu)\right] \right\} dT_e, \tag{10}$$

where N_e is the number of electrons in target, Φ_ν is the neutrino flux of the Sun, $d\lambda/dE_\nu$ is the differential energy spectrum of the solar neutrinos, $\frac{d\sigma_e}{dT_e}$ ($\frac{d\sigma_{\mu,\tau}}{dT_e}$) is the differential scattering cross section as a function of electron kinetic energy for ν_e ($\nu_{\mu,\tau}$), and P_{ee} is the ν_e survival probability. The recoiled electron spectra of the solar neutrinos can be seen in Fig. 13. The number of electron candidates for the high and low metallicity hypotheses and the effective number of electron candidates with a 200 keV energy threshold are shown in Tab. 2, where the number of electrons per 100 tons is assumed to be 3.307×10^{31} [17].

Without a precise electron direction measurement and reconstruction, it is very hard to estimate the original neutrino energy (see Fig. 12). The smooth MSW oscillation transition in neutrino energy presents itself differently in electron kinetic energy. In Fig. 14, the observed electron kinetic energy spectra with and without the oscillation effect are shown together and the relative ratio between them is also shown next to it.

2.1.6 Detector response model

Three types of target materials are considered for detecting the recoiled electron from the neutrino electron elastic scattering.

Liquid scintillator featuring with its high light yield, low detecting threshold, has been successfully used in the Borexino experiment [17], and is an option to be used in the SNO+ experiment. The liquid scintillator detector response can be approximated by a simple characteristic resolution function. The non-uniform and non-linear detector energy responses can both be calibrated back, so they are not necessary to be included in this study. The SNO+ experiment inherited the almost doubled photocathode coverage from the SNO experiment [41] than the Borexino [42], then a doubled light yield is considered possible in this study. Liquid scintillator is used as a reference material for this study.

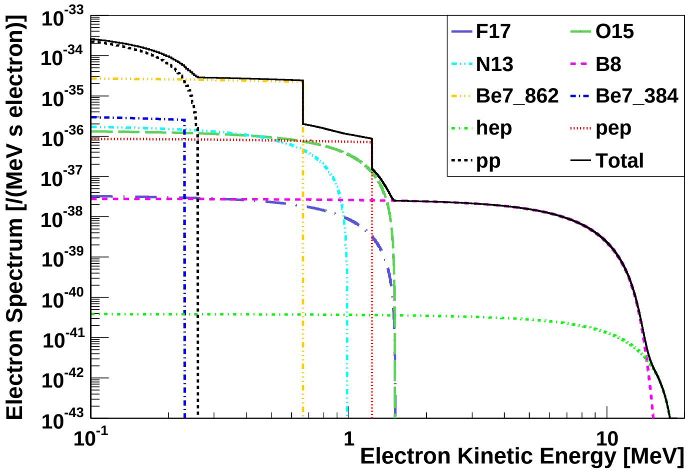

Figure 13: (Color online) Kinetic energy spectra of recoiled electron for each solar neutrino component, and the total electron kinetic energy spectrum, where the MSW oscillation and the high metallicity hypotheses are both considered.

Electron Event Rate [/day 100 ton]	>0 keV (GS98) high metallicity	>0 keV (AGS09) low metallicity	>200 keV (GS98) high metallicity	>200 keV (AGS09) low metallicity
pp	132.59 ± 0.80	133.70 ± 0.80	4.557 ± 0.027	4.595 ± 0.028
^{7}Be (0.38 MeV)	1.93 ± 0.13	1.76 ± 0.12	0.228 ± 0.016	0.208 ± 0.015
^{7}Be (0.86 MeV)	46.9 ± 3.3	42.8 ± 3.0	31.6 ± 2.2	28.8 ± 2.0
pep	2.735 ± 0.033	2.792 ± 0.034	2.244 ± 0.027	2.291 ± 0.028
^{13}N	2.45 ± 0.34	1.80 ± 0.25	1.48 ± 0.21	1.09 ± 0.15
^{15}O	2.78 ± 0.42	1.95 ± 0.29	2.03 ± 0.31	1.42 ± 0.21
^{17}F	0.069 ± 0.012	0.0426 ± 0.0072	0.0506 ± 0.0086	0.0312 ± 0.0053
^{8}B	0.443 ± 0.062	0.364 ± 0.051	0.427 ± 0.060	0.351 ± 0.049
hep	0.0009 ± 0.0003	0.0009 ± 0.0003	0.0009 ± 0.0003	0.0009 ± 0.0003

Table 2: Expected electron event rates with no threshold or 200 keV threshold when the effect of MSW neutrino oscillation is considered for both the high and low metallicity hypotheses. The error is from the solar model prediction only.

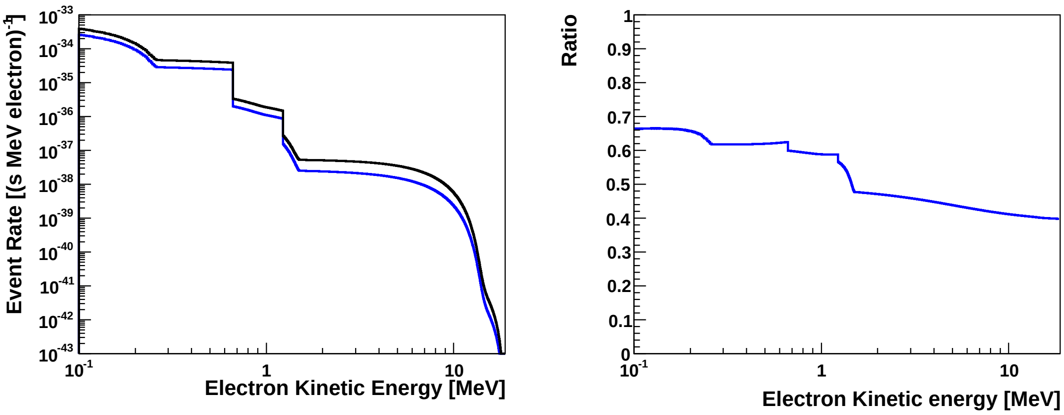

Figure 14: (Color online) Left: recoiled electron kinetic energy spectrum with (blue) and without (black) oscillation. Right: the relative ratio between them.

Water is another option under our consideration. Although its detecting threshold, which is currently about 3 MeV reached by the Super Kaminokande experiment [43], is high when comparing to the energy range of the main physics, it is still interesting, because the improvement on PMT technique and electronics may help to overcome the major high noise issue.

A new technology of water-based scintillator [44] is also interesting. It may be used to separate scintillating and Cherenkov lights and to provide an additional information for energy reconstruction and background suppression.

Three typical energy resolutions were tested in this study and their values and corresponding resolution functions are summarized in table 3.

Light yield	Resolution function (dE/E)	Experiment
200 PE/MeV	$1/\sqrt{200E/\text{MeV}}$	
500 PE/MeV	$1/\sqrt{500E/\text{MeV}}$	Borexino like
1,000 PE/MeV	$1/\sqrt{1000E/\text{MeV}}$	SNO+ like

Table 3: Three types of light yields and resolution functions for detector response.

2.1.7 Background assumption

There are mainly three categories of backgrounds. 1) Cosmic-ray muon induced spallation backgrounds. With the overburden of Jinping, these backgrounds will be reduced by a factor of 200 than those in Borexino or a factor of 2 in SNO. 2) Internal radioactive beta or gamma backgrounds. These are the residual background remaining in detecting material and are not related to the depth, but can be reduced by purification. They are assumed to be at the same level as Borexino. 3) Environment radioactive background. They present as external gammas for a central detector volume. Borexino background rates are scaled according to surface area.

For simplicity, to get the total visible energy, no quenching is considered in the following study, so that for sequential beta and gamma decays, all gamma energies and beta kinetic energies are added linearly without the need of the detail of the decay structure of excited states. For positrons from beta+ decay, two times of electron mass are added for positron annihilation.

The visible energy spectra for category 1) and 2) are shown in Fig. 15. External gamma background is modeled by an exponential distribution, motivated by [17]. An example energy distribution for the 2.6 MeV gamma background from the external ^{208}Tl is also shown in Fig. 15, where the decay constant is assumed to be 0.4 MeV, which is related to the gamma ray attenuation length and fiducial volume buffer dimension.

A summary of the event rates of all considered backgrounds can be found in table 4. Details are in below.

The Borexino I ^{7}Be refers to the analysis result of the Borexino phase I ^{7}Be measurement [17, 45, 46], from which the fiducial volume mass, live time, and background rates of ^{14}C, ^{85}Kr, ^{210}Bi, and ^{11}C are extracted and values for ^{14}C and ^{11}C are used for Jinping study. Other backgrounds, ^{10}C, ^{208}Tl, ^{11}Be, and Ext-^{208}Tl, not so relevant for ^{7}Be study are extracted from the other references discussed below.

The Borexino I pep refers the analysis result of the Borexino phase I pep measurement [17, 47], where the data of 598.3 live days is scaled down by 48.5% considering the final selection efficiency. With the technique of threefold coincidence (TFC), the background rate of ^{10}C is suppressed. The ^{10}C background rate without the TFC technique is taken as a standard value of the Borexino experiment, and then scaled to Jinping. The most significant and presentative external gamma

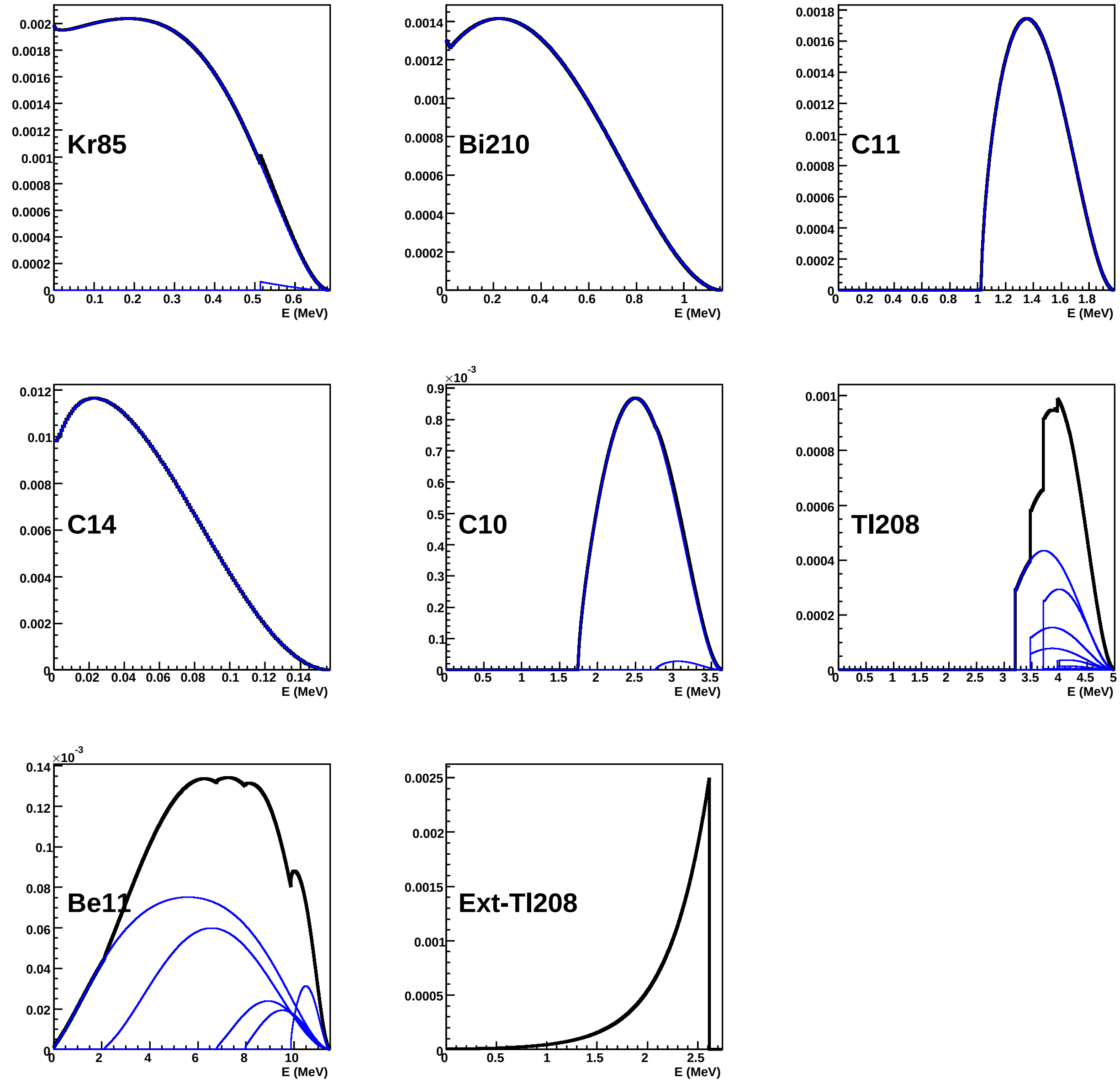

Figure 15: (Color online) Visible energy spectra for cosmic-ray muon induced, and residual radioactive backgrounds (first 7 plots). The black is for the total visible energy spectrum and the blue ones are for sub branches. Visible energy spectrum for external 2.6 MeV gamma background (^{208}Tl) (last plot).

background, Ext-^{208}Tl, as a major background is extracted from this analysis and used for Jinping study.

Borexino I ^{8}B is for the ^{8}B analysis in Borexino phase I [48], where the energy spectrum >3 MeV is discussed. The reported rates of the high energy backgrounds ^{208}Tl and ^{11}Be are taken to be the standard values for the Borexino experiment, and used for Jinping study.

The second phase of the Borexino experiment has a much lower ^{85}Kr and ^{210}Bi background rates [49]. A sample with double live days of data is assumed comparing the phase one analysis. Background rates of ^{85}Kr and ^{210}Bi are used for Jinping study.

For the SNO+ proposal, the fiducial volume mass is 500 tons [50] considering a 4 m buffer, and

	Mass	Time	Resolution	^{14}C	^{85}Kr	^{210}Bi	^{11}C	^{10}C	^{208}Tl	^{11}Be	Ext-^{208}Tl
	[100 ton]	[day]	[PE/MeV]			[Counts/day/100 ton]					
Borexino I ^{7}Be	0.7547	740.7	500	3.46×10^6	31.2	41.0	28.5	0.62	0.084	0.032	2.52
Borexino I pep	0.7130	290.2	500	3.46×10^6	31.2	41.0	2.48	0.18	0.084	0.032	2.52
Borexino I ^{8}B	1	345.3	500	3.46×10^6	31.2	41.0	28.5	0.62	0.084	0.032	2.52
Borexino II ^{7}Be	0.7547	1480	500	3.46×10^6	1	25.0	28.5	0.62	0.084	0.032	2.52
Borexino II pep	0.7130	580	500	3.46×10^6	1	25.0	2.48	0.18	0.084	0.032	2.52
Borexino II ^{8}B	1	690	500	3.46×10^6	1	25.0	28.5	0.62	0.084	0.032	2.52
SNO+	5	1500	1000	3.46×10^6	1	25.0	0.29	0.0062	0.084	0.00032	1.47
Jinping	10	1500	test	3.46×10^6	1	25.0	0.15	0.0031	0.084	0.00016	1.17

Table 4: A summary of all known running or planed solar neutrino experiments including fiducial mass, live time, and all considered backgrounds. See the text in Sec. 2.1.7 for the references and calculation methods for each experiment or analysis.

data taking time is about 5 years. The ^{85}Kr and ^{210}Bi background rates are the same as Borexino II. The cosmogenic backgrounds, ^{11}C, ^{10}C, and ^{11}Be are scaled by a factor of 1/100. Internal background ^{208}Tl is taken to be the same as Borexino. However, the Ext-^{208}Tl background rate per 100 tons is obtained by scaling the Borexino result according to their surface area ratio and the detector mass ratio.

2.1.8 Total spectrum

An example plot of the total expected spectrum including all the neutrino and background components at Jinping with 1 kton liquid scintillator scheme, 1,500 live days of data, and 500 PE/MeV of the detector response is shown in Fig. 16. Simulated samples are fitted and analyzed for each physics topic below and the corresponding discovery sensitivities will be reported.

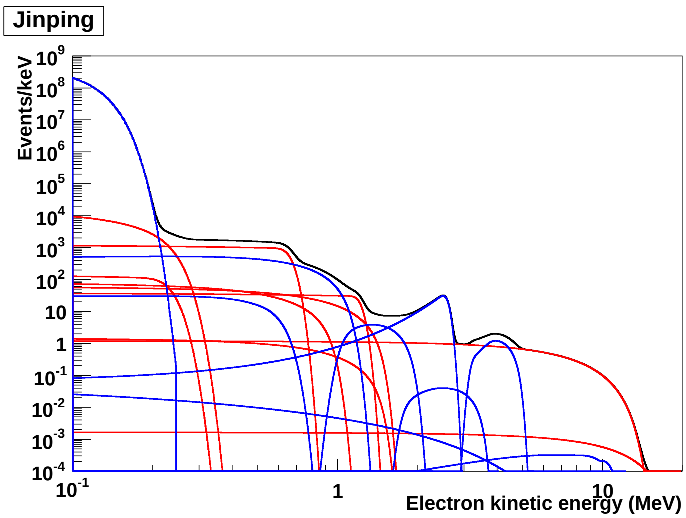

Figure 16: (Color online) An example plot of the total expected spectrum including all the neutrino (red) and background (blue) components at Jinping with 1 kton liquid scintillator scheme, 1,500 live days of data, and 500 PE/MeV og detector response .

2.1.9 Systematics on fluxes measurement

Two types of systematic uncertainties are considered for the measurement on the neutrino flux of the Sun. One is the fiducial volume definition, which is only related to the bias of vertex reconstruction rather than the resolution. A 1% systematic uncertainty is assumed for the fiducial volume cut. The other one is from the energy response of detector. With the experience of the Borexino experiment and the recent Daya Bay experiment [51], the uncertainty from the non-linearity and non-uniformity effect in the energy reconstruction is believed to be able to be controlled to the level of 1%. With a large data sample expected at Jinping, we assume there is no fitting procedure error as induced by Borexino analysis. In total, 1.5% systematic uncertainty will be assigned to all the flux measurements.

2.2 Precision of each solar neutrino component

Several Jinping samples, which are simulated according to table 2 with several different energy resolution models, are fitted. Fitting examples are shown in Fig. 17. The ^{7}Be 0.38 MeV line to 0.86 MeV ratio is fixed according to table 1. The shape of ^{15}O and ^{17}F are not distinguishable and only ^{15}O component is considered in the fitter. The hep neutrino is not significant in the fit and not used. The statistical and systematic precisions of all solar neutrino components for the high and low metallicity models are shown in table 5.

Relative error	Statistical			Systematic
	200 PE/MeV	500 PE/MeV	1000 PE/MeV	
pp	0.02	0.008	0.006	0.015
^{7}Be (0.86 MeV)	0.008	0.006	0.006	0.015
pep	0.06	0.04	0.04	0.015
^{13}N	NA (NA)	0.5 (NA)	0.2 (0.4)	0.015
^{15}O	0.3 (0.4)	0.2 (0.3)	0.1 (0.2)	0.015
^{8}B	0.02	0.02	0.02	0.015

Table 5: Measurement precision of the flux for each solar neutrino component with different resolution setup. Errors are all expressed in relative terms for high metallicity and the ones in the parentheses are for low metallicity assumption if they are significantly different. The ^{7}Be 0.38 MeV line to 0.86 MeV ratio is fixed according to table 1. The shapes for ^{15}O and ^{17}F can not be distinguished so that ^{15}O here represents the sum of them. The hep neutrino is not in the fit for its low statistics. If one error is over 0.5, then it is marked as NA.

2.2.1 Improvement of known neutrino components

pp neutrino As shown in Fig. 17, the electron energy from the pp neutrino elastic scattering is slightly higher than that from the main background ^{14}C, and the best signal region for detecting the pp neutrinos is at 0.2 - 0.3 MeV. The statistical uncertainty in the measurement of the pp neutrino flux is very sensitive to the energy resolution of the detector, which can reach 1% with the 500 PE/MeV light yield. The total uncertainty will be dominated by the systematic uncertainty. It is expected to control the dominant systematic uncertainty and reduce the total uncertainty down below 1%, and this will help to find the difference between the neutrino luminosity and the light luminosity.

^{7}Be neutrino ^{7}Be and ^{8}B neutrinos are critical to distinguish the high and low metallicity hypotheses. The ^{7}Be neutrino flux can be measured statistically better than 1%, which is not

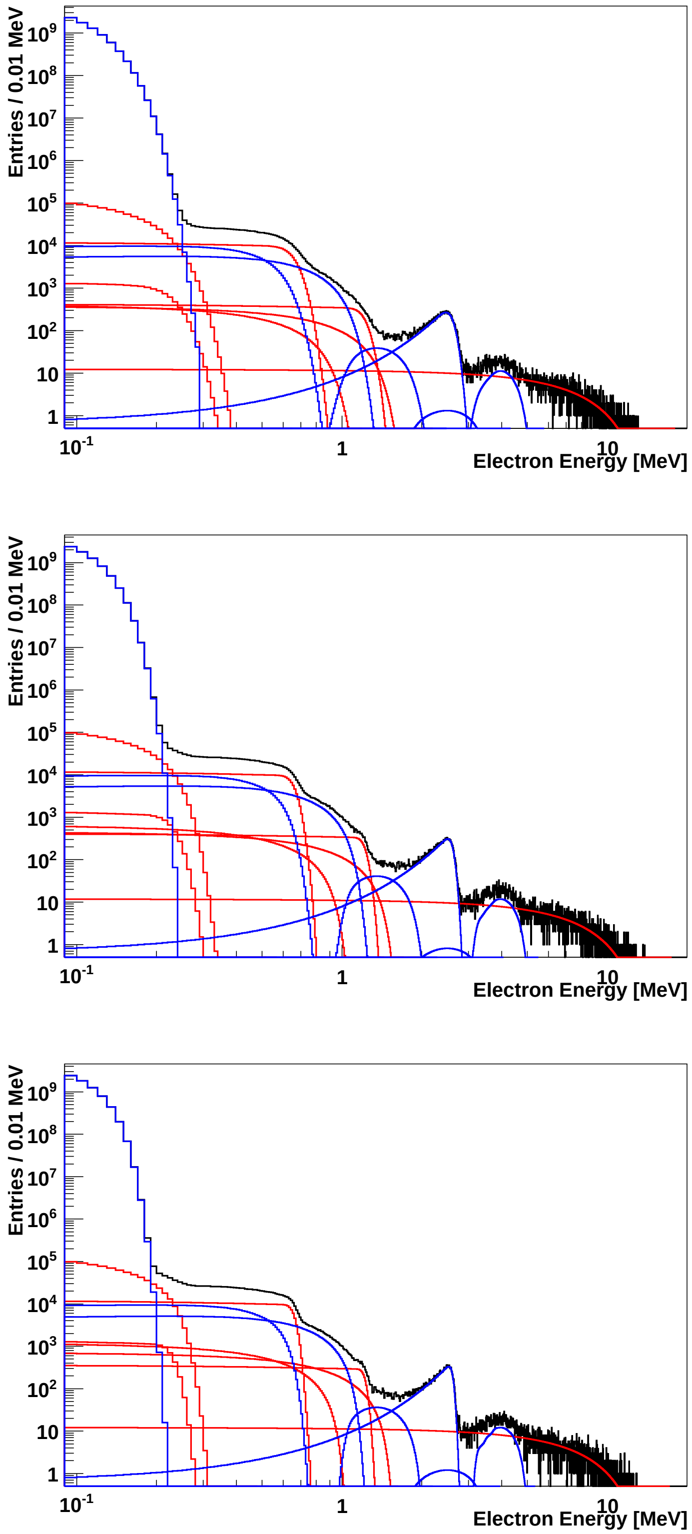

Figure 17: (Color online) From top to bottom are the fit results for 200, 500, and 1,000 PE/MeV simulations, respectively (GS98 high metallicity). ^{7}Be and pep neutrinos have a sharp edge structure and ^{8}B neutrino have a very broad distribution, so that they are not so sensitive to detector resolution. But pp and CNO neutrinos rely on the precise determination of all other neutrino and background components, so they are sensitive to detector resolution.

sensitive to the three resolution options considered due to its sharp turn. The total flux uncertainty is dominated by the systematic uncertainty.

^{8}B neutrino ^{8}B neutrinos suffer the largest matter effect, which is sensitive to the vaccum-matter transition phase and the day-night flux asymmetry. The relatively high energy of ^{8}B neutrinos lets them less contaminated by other backgrounds, and because of the broad energy spectrum, the study of ^{8}B neutrinos does not rely on the energy resolution much. The statistical precision on the flux of ^{8}Be neutrinos is expected to be about 2% , which is limited by the target mass, and is comparable to the systematic uncertainty.

pep neutrino The distinguishable structure of pep neutrino spectrum, like ^{7}Be neutrino, makes it is easy to identify. With the three energy resolution options considered, it can all reach 6%. The pep neutrino is one of the key point in determining the solar model and vacuum-matter oscillation transition.

2.2.2 Discovery of CNO neutrino

CNO neutrino The flux of CNO neutrinos strongly depends on the metallicity hypotheses and itself is an very interesting subject since CNO neutrinos are from the main fueling process of high temperature stars, while the pp process is dominant in the Sun, which has relatively low temperature. Both ^{13}N and ^{15}O neutrinos hide under the ^{7}Be and pep neutrinos, and ^{85}Kr and ^{210}Bi backgrounds. An effective identification of the other neutrinos and backgrounds will help to resolve the CNO neutrinos, and will thus rely on the energy resolution. With a resolution of 500 PE/MeV, a discovery of ^{15}O neutrinos will be possible and with a resolution of 1,000 PE/MeV, the ^{13}N neutrino may be distinguished.

2.3 Matter-vacuum transition phase

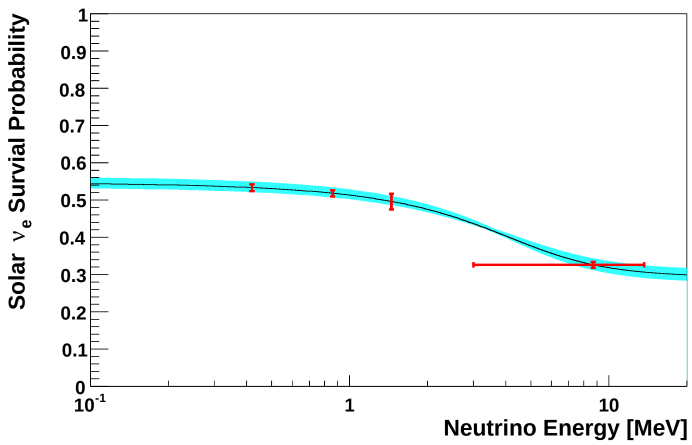

Figure 18: (Color online) The transition of oscillation probability from the matter effect to the vacuum effect as a function of neutrino energy. This plot is for Jinping experiment with a simulation of 1,500 days and a resolution of 500 PE/MeV and the low metallicity assumption, where the solid line is for the theoretical prediction, the shaded area is obtained by marginalizing θ_{12}, θ_{13}, and Δm^2_{12} according to the present experimental uncertainty, the four points with error bars are the simulation results for pp, ^{7}Be, pep, and ^{8}B, in which the central values are set to the true ones, while the error bars include both statistical and systematic uncertainties.

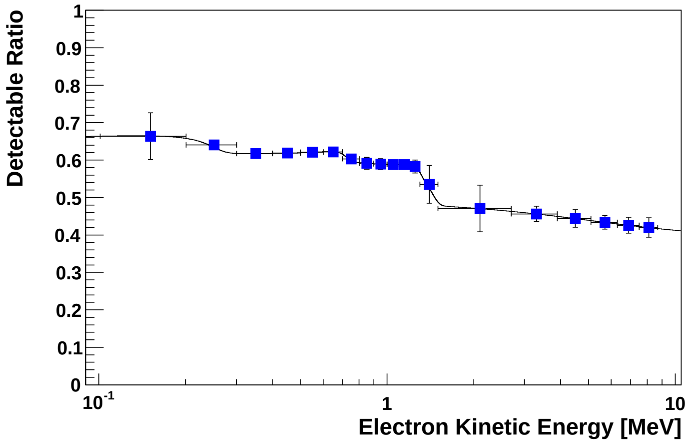

Figure 19: (Color online) The transition of oscillation probability from the matter effect to the vacuum effect as a function of kinetic energy of recoiled electrons. This plot is for Jinping experiment with a simulation of 1,500 days and a resolution of 500 PE/MeV and the low metallicity assumption, where the solid line is for the theoretical prediction and the dots with error bars are for the simulation. Errors include all the statistical error from both backgrounds and signals.

The transition of oscillation probability from the matter-governed region to the pure vacuum-like region is a very interesting phenomenon of the MSW effect as shown in Fig. 9 and 14, which has been studied by Borexino [17, 48], Super Kaminokande [43] and SNO [50], however, experimentally it is still loosely constrained. With Jinping simulation, the expected flux measurements are compared with the predictions on neutrino energy and recoiled electron kinetic energy, which are shown in Fig. 18 and 19, respectively. For Fig. 19, the uncertainty of each bin is conservatively treated as the square root of the full statistics of each bin including all backgrounds and signals, and, for a better performance of looking, the binning ranges are also adjusted according to the statistics.

2.4 Day-night asymmetry

After solar neutrinos passing through the Earth, electron neutrinos may be regenerated because of the MSW matter effect [26], whose flux is slightly higher than the day-time survival probability. The survival probability is very sensitive to Δm^2_{21} and nearby surface density profile of the Earth [27, 28], which cause a day-night asymmetry in counting the solar neutrinos. The asymmetry can vary from 1% to 3%. The asymmetry with the parameters considered here is shown in Fig. 20. The sensitivity of Jinping experiment for the asymmetry above 3 MeV can be directly estimated with the expected statistics of ^8B events, since the background beyond 3 MeV is not significant. The separation between the fluxes in the day and night is

$$s = 2(N - D)/(N + D), \tag{11}$$

where N and D are the signal event counts during the night and day. The uncertainty of s is

$$\sigma_s \approx 2/\sqrt{N + D} = 2/\sqrt{N_{B8}}, \tag{12}$$

where N_{B8} is the total statistics of ^8B neutrino events. According to Table 2, with a 5-year data-taking, a kiloton detector is insufficient to make a conclusive measurement on the day-night asymmetry.

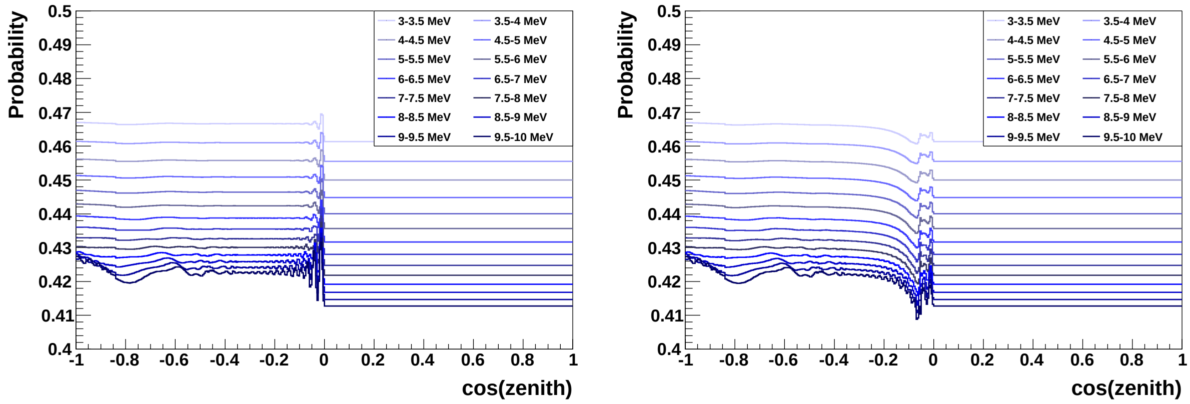

Figure 20: (Color online) Day-night asymmetry for a continental site (left) and an ocean site (right).

2.5 Metallicity problem

With the precise measurements on the ^7Be and ^8B neutrino fluxes shown in table 5, it is possible to distinguish two metallicity hypotheses from each other. The comparison between the predictions and the possible precision reached by Jinping experiment is shown in Fig. 21. With the measured fluxes of other neutrino components, pep and CNO, the sensitivity can be further increased.

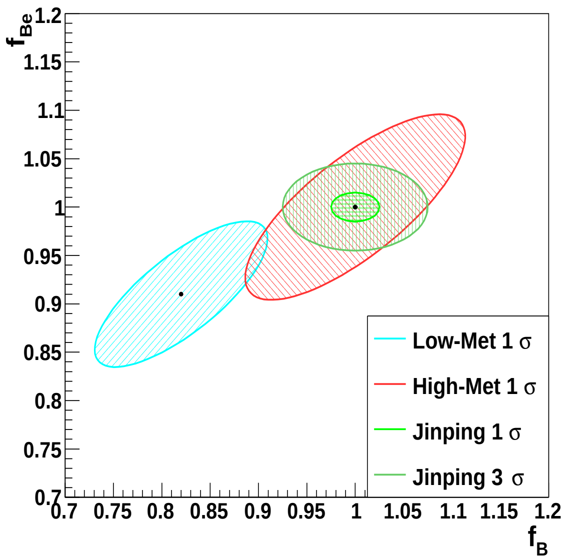

Figure 21: (Color online) Jinping's potential in distinguishing the low and high metallicity hypotheses, where f_{Be} and f_B are either the Jinping measurements or the model predictions of ^{7}Be and ^{8}B fluxes normalized to the high metallicity predictions. For Jinping measurements, the central values are set to the high metallicity values and the error bars include both statistical and systematic uncertainties.

2.6 Summary

A kiloton fiducial mass detector running over 5 years is very promising to make a discovery of CNO neutrinos, and to significantly improve the precision of pp, ^{7}Be, pep neutrino fluxes. It can also provide a much stronger experimental constrain on the vacuum-matter transition of MSW effect, and have the capability to distinguish the high and low metallicity hypotheses. Due to the target mass, physics relying on the statistics of ^{8}B neutrinos cannot be precisely probed, for example, the day-night asymmetry. In this section, we haven't touched the subject of possible improvement on the measurement of neutrino mixing angles and the possibility to rule out other new physics.

References

[1] J. Bahcall, arXiv:astro-ph/0009259 (2000).

[2] W.C. Haxton, Nature **512**, 378 (2014).

[3] A B McDonald, New Journal of Physics **6**, 121 (2004).

[4] Solar neutrinos the first thirty years, edited by J. Bahcall, *et al.*, Westview Press (1994).

[5] J. Bahcall home page: http://www.sns.ias.edu/~jnb/.

[6] B.T. Cleveland *et al.*, Astrophys. J. **496**, 505 (1988).

[7] J.N. Abdurashitov *et al.*, (SAGE Collaboration), Phys. Rev. **C80**, 015807 (2009).

[8] P. Anselmann *et al.*, (GALLEX Collaboration), Phys. Lett. **B285**, 376 (1992).

[9] M. Altmann *et al.*, (GNO Collaboration), Phys. Lett. **B616**, 174 (2005).

[10] Y. Fukuda *et al.*, (Kamiokande Collaboration), Phys. Rev. Lett. **77**, 1683 (1996).

[11] S. Fukuda *et al.*, (Super-Kamiokande Collaboration), Phys. Lett. **B539**, 179 (2002).

[12] Q.R. Ahmad *et al.*, (SNO Collaboration), Phys. Rev. Lett. **89**, 011301 (2001).

[13] B. Pontecorvo, Sov. Phys. JETP **6**, 429 (1957) and **26**, 984 (1968).

[14] Z. Maki, M. Nakagawa, and S. Sakata, Prog. Theor. Phys. **28**, 870 (1962).

[15] L. Wolfenstein, Phys. Rev. **D17**, 2369 (1978).

[16] S.P. Mikheev and A.Y. Smirnov, Sov. J. Nucl. Phys. **42**, 913 (1985); Nuovo Cimento **9C**, 17 (1986).

[17] G. Bellini, *et. al.* (Borexino Collaboration), Phys. Rev. **D89**, 112007 (2014).

[18] W.C. Haxton, R.G. Hamish Robertson, and A. Serenelli, Annu. Rev. Astron. Astrophys. **51**, 21 (2013).

[19] J. Bahcall and C. Peña-Garay, New J. of Phys. **6**, 63 (2004).

[20] J. Bahcall and R. K. Ulrich, Rev. Mod. Phys. **60**, 297 (1988).

[21] J. Bahcall and C. Peña-Garay, JHEP **11**, 004 (2003).

[22] W.C. Haxton, R.G. and A. Serenelli, Astrophys. J. **687**, 678 (2008).

[23] P. C. de Holanda and A. Yu. Smirnov, Phys. Rev. **D69**, 113002 (2004).

[24] R. Bonventre, *et. al.*, Phys. Rev. **D88**, 053010 (2013).

[25] A. Friedland, C. Lunardini, and C. Peña-Garay, Phys. Lett. **B594**, 347 (2004).

[26] J. N. Bahcall and P. I. Krastev, Phys. Rev. **C56**, 2839 (1997).

[27] J. N. Bahcall, P. I. Krastev, and A. Yu. Smirnov, Phys. Rev. **D60**, 093001 (1999).

[28] A. Renshaw, *et. al.*, Phys. Rev. Lett. **112**, 091805 (2014).

[29] A. Serenelli, *et. al.*, Astrophys. J. **705**, L123 (2009).

[30] A. Serenelli, W. C. Haxton, and C. Peña-Garay, Astrophys. J. **743**, 24 (2011).

[31] M. Asplund, S. Basu, J.W. Ferguson, and M. Asplund, Astrophys. J. Lett. **705**, L123 (2009).

[32] P.C. de Holanda, Wei Liao, and A.Yu. Smirnov, Nucl. Phys. **B702**, 307 (2004).

[33] J. Bahcall, M. H. Pinsonneault, and S. Basu, Astrophys. J. **555**, 990 (2001).

[34] G. L. Fogli, E. Lisi, D. Montanino, and A. Palazzo1, Phys. Rev **D62**, 113004 (2000).

[35] E. Lisi, A. Marrone, D. Montanino, A. Palazzo, and S. T. Petcov, Phys. Rev **D63**, 093002 (2000).

[36] S. Goswami and A. Y. Smirnov, Phys. Rev. **D72**, 053011 (2005).

[37] C. Giunti, *et. al.*, Nucl. Phys. **B521**, 3 (1998).

[38] Theory of the earth, D. L. Anderson, Blackwell Scintific Publications .

[39] J. Hosaka, *et. al.* (Super-Kamiokande Collaboration), Phys. Rev. **D73**, 112001 (2006).

[40] C. Giunti and C. W. Kim, Fundamentals of Neutrino Physics and Astrophysics, Oxford university press (2007).

[41] B. Aharmim, *et. al.* (SNO Collaboration) Phys. Rev. **C72**, 055502 (2005).

[42] L. Oberauera, C. Grieba, F. Feilitzscha, and I. Mannoc, Nucl. Instr. and Meth. A **530**, 453 (2004).

[43] K. Abe, *et. al.* (Super-Kamiokande Collaboration), Phys. Rev. **D83**, 052010 (2011).

[44] M. Yeh, *et al.*, Nucl. Inst. & Meth. **A660**, 51 (2011).

[45] C. Arpesella, *et. al.* (Borexino Collaboration), Phys. Rev. Lett. **101**, 091302 (2008).

[46] G. Bellini, *et. al.* (Borexino Collaboration), Phys. Rev. Lett. **107**, 141302 (2011).

[47] G. Bellini, *et. al.* (Borexino Collaboration), Phys. Rev. Lett. **108**, 051302 (2012).

[48] G. Bellini, *et. al.* (Borexino Collaboration), Phys. Rev. **D82**, 033006 (2010).

[49] G. Bellini, *et. al.* (Borexino Collaboration), Nature **512**, 383 (2014).

[50] B. Aharmim, *et. al.* (SNO Collaboration), Phys. Rev. **C88**, 025501 (2013).

[51] F. P. An, *et. al.* (Daya Bay Collaboration), Phys. Rev. Lett. **112**, 061801 (2014).

3 Supernova relic neutrino

Supernova relic neutrino (SRN) background, also known as diffuse supernova neutrino background, is highly desired by neutrino astronomy and neutrino physics. When a massive star ($> 8M_{\odot}$) is on its way to the end, it collapses into a high-density and -pressure core, and the core has a possibility to become a supernova. An enormous amount of neutrinos are emitted when the supernova explodes and carry away almost 99% of its gravitational energy. The chance to detect supernova burst neutrinos is rather rare, probably once per one century [1], and the neutrinos from SN1987A so far are the only ones being recorded. However neutrinos emitted from past core-collapse supernovae accumulated and formed a continuum diffused background, and the chance to discover supernova relic neutrinos is relatively higher. An observation of supernova relic neutrinos will reveal the process of stellar evolution and the history of our universe, and it is a unique tool for astronomy research. Experimental searches have been carrying on by Super Kaminokande [2, 3, 4], KamLAND [5], Borexino [6], and SNO [7]. However, no any SRN signal has been found yet. After the discovery of solar neutrinos, diffused supernova relic background as another extraterrestrial neutrinos source is attracting more and more attention for experimental efforts. In this section, we will estimate the prospect of Jinping underground experiment.

3.1 SRN Models

The SRN flux and spectrum prediction are both based on several theoretical inputs [8]: supernova neutrino emission spectrum, cosmic supernova rate, and neutrino oscillation and interaction. Many models have been proposed to predict the SRN flux and spectrum. In this analysis we will use the following models to project the sensitivity at Jinping: LMA[9], Constant SN[10], Cosmic gas[11], Chemical evolution[12], Heavy metal[13][14], Population synthesis[15], HBD 6 MeV[16], Star formation rate[17], and Failed SN[18]. The most interested $\bar{\nu}_e$ energy spectra from the above models are shown in Fig. 22. The average energy of supernova burst neutrinos is highly red-shifted from 20 MeV to below 5 MeV for all models, and the total flux predictions among the models are within one order of magnitude.

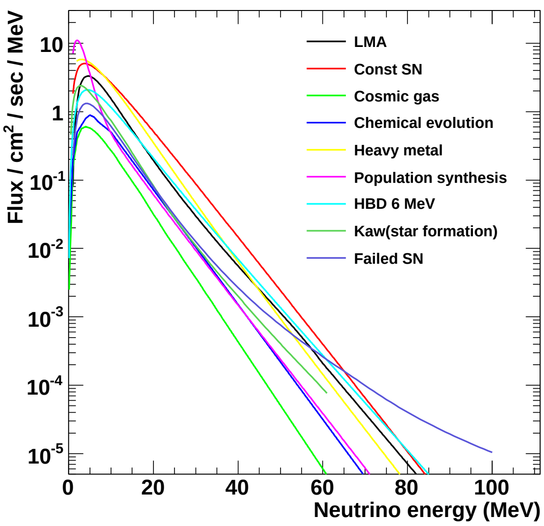

Figure 22: (Color online) Model dependence of $\bar{\nu}_e$ energy spectra for supernova relic neutrinos

3.2 Detection

There are three flavors of neutrinos and anti-neutrinos in SRN, among which $\bar{\nu}_e$ is mostly likely to be detected due to its large cross section of inverse beta decay (IBD), $\bar{\nu}_e + p \to e^+ + n$, in hydrogen (free proton) rich material within the energy region of several tens of MeV.

Liquid scintillator and water-based liquid scintillator (WbLS) [19] are studied as the detecting material, since they all have a high efficiency for tagging the delayed neutron, which has a coincidence with the prompt e^+ signal generated through an IBD chain, providing a powerful rejection to accidental backgrounds [5, 6, 4]. Gadolinium loaded water [20] is temporarily skipped in this study.

In liquid scintillation detectors, the high dE/dx deposited by proton and alpha makes them possible to be differentiated from beta and gamma by a pulse shape analysis. In WbLS, low energy proton, alpha, and muon in the interested energy region cannot produce Cherenkov light in the search of SRN. We think WbLS with the capability of distinguish Cherenkov and scintillation light can provide a more powerful suppress to backgrounds. In this regards, these water detectors will work more efficiently than the scintillator detectors do.

The SRN event rate to be detected via IBD can be calculated by

$$\frac{\mathrm{d}R}{\mathrm{d}E} = \frac{\mathrm{d}\phi_\nu}{\mathrm{d}E} \times \sigma(E) \times N_p \times T, \tag{13}$$

where E is the neutrino energy, $\frac{\mathrm{d}\phi_\nu}{\mathrm{d}E}$ is a model-depedence prediction for $\bar{\nu}_e$ flux, $\sigma(E)$ represents the differential IBD cross section [21], N_p is the number of free protons in the target, and T is the data-taking time. The threshold of the reaction is 1.8 MeV, and the kinetic energy of the neutrino is almost all transferred the positron. The visible energy of the reaction is the kinetic energy of the positron plus two annihilation photons and can be related to the neutrino energy by

$$E_{vis} = E - 0.78\mathrm{MeV}. \tag{14}$$

The differential visible energy spectra per kiloton detector per year is shown in Fig. 23, and the expected event rates in the most interested E_{vis} region of 10 - 30 MeV are listed in table 6.

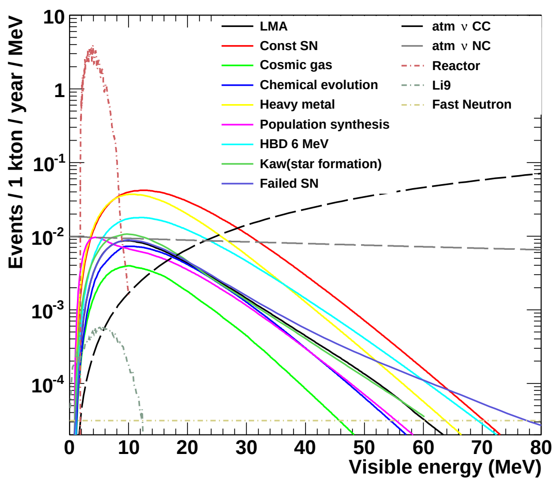

Figure 23: (Color online) Visible energy spectra of supernova relic neutrinos for different models and visible energy spectra of all possible backgrounds.

3.3 Backgrounds

There are mainly six types of backgrounds for SRN detection: 1) accidental coincidence; 2) reactor $\bar{\nu}_e$; 3) fast neutrons induced by energetic cosmic-ray muons; 4) ^{9}Li or ^{8}He radiative isotopes induced by energetic cosmic-ray muons; 5) atmospheric neutrino background through a charge current (CC) process; and 6) atmospheric neutrino background through a neutral current (NC) process. The estimation of their rates are explained below.

3.3.1 Accidental coincidence

Accidental coincidence background is considered as negligible given the expected location and cleanness of neutrino detector.

3.3.2 Reactor $\bar{\nu}_e$

Reactor $\bar{\nu}_e$ events are identical to the SRN signal except for the energy spectrum, which is below 10 MeV as shown in Fig. 23. A requirement on energy above 10 MeV together with the fact that there is no nuclear power plant in close proximity will significantly suppress the reactor $\bar{\nu}_e$ background down to a negligible level.

3.3.3 Fast Neutron

Cosmic-ray muon or its secondary products may collide with the nuclei in target or surrounding materials, and knock out energetic fast neutrons. The recoiled proton by the fast neutron can minic a prompt positron signal, while the scattered neutron is quickly thermalized and captured by atom, forming a delayed neutron signal.

The fast neutron background is scaled from KamLAND measurement $(3.2 \pm 3.2)/(4.53$ kton-year$) = (0.7 \pm 0.7)/$kton-year [5] to Jinping site. Muon rate at Jinping is about 1,000 times lower than KamLAND, as shown in Fig. 6. As a result, the fast neutron background is reduced to a rather low level, which is estimated to be $(0.7 \pm 0.7) \times 10^{-3}/$kton-year for those with visible energy from 10 to 30 MeV.

Some minor factors may be considered in order to give a more precise estimation. Usually a neutrino detector is perfect for giving a muon self-veto. Muons passing surrounding insensitive materials, i.e. rock, are the main cause for fast neutrons to be problematic. A more careful consideration should scale according to surface area ratio. Since KamLAND detector mass, 1 kton, may be close to Jinping expectation, this is a only minor correction. Secondly, the fast neutron yield increases as an exponential function of muon energy, $yield = (E_{Jinping}/E_{KamLAND})^{0.77}$ [22]. With the 351 GeV of average muon energy at Jinping and 260 GeV at KamLAND this increase is insignificant. The shape of the prompt signal for fast neutron background has been understood [23, 24] and is basically a flat distribution below 100 MeV as shown in Fig. 23.

3.3.4 Spallation ^{9}Li/^{8}He

The spallation products ^{9}Li/^{8}He induced by cosmic-ray muons can decay via a beta delayed neutron emission. The beta signal together with the delayed neutron signal have a similar signature as the IBD signal. The half-life and Q-value of ^{9}Li are 173 ms and 14 MeV, respectively, and 119 ms and 11 MeV for ^{8}He, respectively. The visible energy spectra of these two background sources are shown in Fig. 23. It is noted that ^{9}Li/^{8}He backgrounds are usually generated locally and won't travel far, and the muons concerned are in the sensitive target region. With an efficient muon detection and long enough veto, they can be effectively removed.

With a suppression factor of 1,000 from the large overburden, KamLAND measurement is scaled to Jinping case, 4.0/4.53 (kton-year)/1000 = 1×10^{-3}/kton-year, for the visible energy within the range from 10 to 30 MeV.

3.3.5 Atmospheric neutrino CC Background

In the energy region interested for the SRN search, another anti-neutrino background source is atmosphere neutrinos[25, 26]. The charged current interaction of atmospheric $\bar{\nu}_e$ is an irreducible background, which, however is not dominant. It is noted that atmospheric $\bar{\nu}_\mu$'s and ν_μ's can produce low-energy muons and delayed neutrons, and thus contaminat the IBD signals. Since the muons can decay to Michel electrons, with a triple coincidence tagging of the prompt event, muon decay, and neutron capture, this background can be rejected efficiently. However, since the inefficiency of the triple tagging and a small fraction of negative muon capture, CC background induced by $\bar{\nu}_\mu$ and ν_μ is dominant. The rate estimation by KamLAND, 0.9/(4.53 kton-year) = 0.2/kton-year, can be applied to Jinping's study. With WbLS, it is assumed to be 0.1/kton-year with the extra capability of particle identification.

3.3.6 Atmospheric neutrino NC Background

The dominant background for SRN is from the neutral current process of atmospheric neutrinos as in KamLAND experiment study. Neutrino at higher energies beyond the signal region may collide with ^{12}C in the target and knock out a neutron. Neutron scattering off protons or particles emitted in the de-excitation of the remaining nucleus cause a prompt signal and the neutron will be the delayed signal.

Some new analysis techniques may help to further suppress this background [27, 28]. To have a delay neutron produced, 2/3 of the chance a ^{11}C at ground state is produced. The half-life and Q-value of the ^{11}C ground state are 20 min and 2 MeV, respectively. A triple tagging of the prompt signal, neutron capture, and ^{11}C decay may help to veto this background, and 5% background survives. For the other 1/3 cases, ^{11}C is at its excited states, and it decays through neutron, proton or alpha emissions. A pulse shape discrimination technique can also be applied, and 1% background may stay. It is expected that KamLAND result 16.4/(4.53 kton-year) = 3.6/kton-year can be suppressed coarsely by a factor of 16=1/(5%+1%) and at Jinping it can reach a level similar to CC background 0.2/kton-year. With WbLS, it is assumed to be 0.1/kton-year with the extra capability of particle identification.

3.4 SRN Detection Sensitivity

The events rate in E_{vis} 10 - 30 MeV are summarized in Table 6, and the results with 10 kton-year and 20 kton-year are also shown. With a water or WbLS target, a neutrino experiment at Jinping has roughly similar signal and background levels, and is very promising to make a discovery with the models with higher predictions.

References

[1] S. Ando, J.F. Beacom, H. Yüksel, Phys. Rev. Lett. **95**, 171101 (2005).

[2] M. Malek *et al.* (Super-Kamiokande Collaboration), Phys. Rev. Lett. **90**, 061101 (2003).

[3] K. Bays *et al.* (Super-Kamiokande Collaboration), Phys. Rev. **D 85**, 052007 (2012).

Expected event rate	1/kton-year	1/(10 kton-year)	1/(20 kton-year)
Signal	0.05 - 0.66	0.5 - 6.6	1 - 13
Accidental coincidence	0	0	0
Reactor background	0	0	0
Fast neutron	0.7×10^{-3}	7×10^{-3}	14×10^{-3}
Spallation ^{9}Li/^{8}He	1×10^{-3}	10×10^{-3}	20×10^{-3}
Atmosphere CC	0.2 (0.1)	2 (1)	4 (2)
Atmosphere NC	0.2 (0.1)	2 (1)	4 (2)
Total background	0.4 (0.2)	4 (2)	8 (4)

Table 6: Event rates for the supernova relic neutrinos and the corresponding backgrounds within E_{vis} in 10 - 30 MeV. For signals, the range of several models' predictions are listed. Background rates are calculated assuming a liquid scintillator target, and the atmospheric CC and NC background rates in parentheses are the results for a water or WbLS target.

[4] H. Zhang *et al.* (Super-Kamiokande Collaboration), Astropart. Phys. **60**, 41 (2015).

[5] A. Gando *et al.* (KamLAND Collaboration), Astrophys. J. **745**, 193 (2012).

[6] G. Bellini *et al.* (Borexino Collaboration), Phys. Lett. B **696**, 191 (2011).

[7] B. Aharmim *et al.* (SNO Collaboration), Astrophys. J. **653**, 1545 (2006).

[8] J. F. Beacom, Annu. Rev. Nucl. Part. Sci. **60**, 439 (2010).

[9] S. Ando, K. Sato and T. Totani, Astropart. Phys. **18**, 307 (2003); J. Phys. Soc. Jpn. (Suppl. B) 77, 9 (2008).

[10] T. Totani and K. Sato, Astropart. Phys. **3**, 367 (1995).

[11] R. A Malaney, Astropart. Phys. **7**, 125 (1997).

[12] D. H. Hartmann and S. E. Woosley, Astropart. Phys. **7**, 137 (1997).

[13] M. Kaplinghat, G. Steigman and T. P. Walker, Phys. Rev. **D 62**, 043001 (2000).

[14] L. Strigari, M. Kaplinghat, G. Steigman and T. Walker, JCAP **0403**, 007 (2004).

[15] T. Totani, K. Sato and Y. Yoshii, Astrophys. J. **460**, 303 (1996).

[16] S. Horiuchi, J. F. Beacom and E. Dwek, Phys. Rev. **D 79**, 083013 (2009).

[17] M. Fukugita and M. Kawasaki, Mon. Not. Roy. Astron. Soc. **340**, L7 (2003).

[18] C. Lunardini, Phys. Rev. Lett. **102**, 231101 (2009).

[19] M. Yeh *et al.*, Nucl. Inst. & Meth. **A660**, 51 (2011).

[20] J. F. Beacom and M. R. Vagins, Phys. Rev. Lett. **93**, 171101 (2004).

[21] P. Vogel and J. F. Beacom, Phys. Rev. D 60 053003 (1999).

[22] S. Abe, *et al.* (KamLAND Collaboration), Phys. Rev. **C 81**, 025807 (2010).

[23] F. P. An, *et al.* (Daya Bay Collaboration), Chin. Phys. C 37, 011001 (2013).

[24] F. P. An *et al.* (Daya Bay Collaboration), Phys. Rev. D (R) 90, 071101 (2014).

[25] O. Peres and A. Smirnov, Phys. Rev. **D 79**, 113002 (2009).

[26] G. Battistoni, A. Ferrari, T. Montaruli and P.R. Sala, Astropart. Phys. **23**, 526 (2005).

[27] R. Moellenberg, Ph. D. thesis, (2009).

[28] M. Wurm, Astropart. Phys. 35, 685 (2012).

4 Supernova burst neutrino

4.1 Introduction

On 1987 February 23, about two dozen supernova (SN) burst neutrinos were observed in the Kamiokande II, IMB, and Baksan experiments from stellar collapse SN 1987A, resulting from the star Sanduleak -69202 exploded in the Large Magellanic Cloud, about 50 kpc away from the Earth [1, 2, 3, 4, 5, 6]. This was the first observation of a supernova neutrino burst and SN 1987A remains the only known astrophysical neutrino source since then except for the Sun. SN burst neutrinos carry away almost all of the gravitational binding energy of a stellar collapse, which are important in studying the core-collapse supernova (ccSN) mechanism [7]. The SN neutrinos can also provide a large range of physical limits on neutrinos [8, 9, 10]. Since ccSN explosions are likely strong galactic sources of gravitational waves, joint observations of both SN burst neutrinos and gravitational waves could provide deep insight into ccSN explosions as well as other fundamental physics [11].

The detection of SN burst neutrinos is so important, however, galactic SN explosions occur with a rate of only a few per century [12], which makes the detection a once-in-a-lifetime opportunity. SN neutrinos are expected to arrive at the Earth a few hours before the visual SN explosion, which enables a precious early warning for a SN observation [7]. The Supernova Early Warning System (SNEWS) [13, 14] collaborates with experiments sensitive to ccSN neutrinos, to provide the astronomical community with a very high-confidence early warning of a SN occurrence, pointing more powerful telescopes or facilities to the event.

In this article, the ccSN model is of 1987A-type, of which all features are compatible with SN 1987A. The SN burst neutrinos has three main phases, which are prompt ν_e burst, accretion, and cooling, respectively [7]. The duration of 10 seconds covers 99% of the luminosity carried off by all flavors of neutrinos and antineutrinos in a SN explosion. The energy spectrum of SN burst neutrinos follows a quasithermal distribution [15],

$$f_\nu(E) \propto E^\alpha e^{-(\alpha+1)E/E_{av}}, \tag{15}$$

where E_{av} is the average energy and α a parameter describing the amount of spectral pinching. In this article, E_{av} is set to be 12.28 MeV and α to be 2.61, which correspond to the cooling phase for SN burst $\bar{\nu}_e$ and thus we choose a 10-second window searching for SN burst neutrinos.

The SN burst neutrinos are emitted in the few-tens-of-MeV range, and the detected neutrinos are dominated by IBD events [16] in the liquid scintillator with a fraction of about 90%. And the coincidence of IBD prompt signal from the positron (a 0.78-MeV downward shift of neutrino energy in general) with the delayed gamma emission ($\sim$2.2 MeV) of the IBD neutron capture on H provides a clear $\bar{\nu}_e$ signature against uncorrelated backgrounds. Based on the chemical decomposition, the IBD cross section, and SN burst neutrino flux [7], the expected number of SN burst neutrinos can be determined

$$N = N_0 \times \frac{L_{\bar{\nu}_e}}{5\times 10^{52}\mathrm{erg}} \times (\frac{10\mathrm{kpc}}{D})^2 \times (\frac{TM}{1\mathrm{kt}}), \tag{16}$$

where N_0 corresponds to the expected number ($\sim$300) of SN burst neutrinos at a distance (D) of 10 kpc and a target mass (TM) of 1 kt. Generally, the luminosity (L) emitted is fixed for the study, which varies with models.

4.2 Supernova Trigger at JinPing

The China JinPing Underground Laboratory is the deepest laboratory across the world with quite low cosmogenically backgrounds. Therefore, the signal-to-background ratio of SN burst neutrinos can be sufficiently high throughout a large range of distances from the Earth. A supernova trigger system can be designed and implemented with one or several detectors to be spatially built (due to the deep rock cover), online looking for any increase of IBD signals within a sliding 10-second window. The experience and techniques could be referred to from the supernova trigger system at Daya Bay [17].

For the IBD selection in a liquid scintillator detector at JinPing, a prompt signal energy cut for SN burst neutrinos is assumed to be 10-50 MeV. Notice that the lower limit can be even lower due to the low background rates, increasing the selection efficiency of SN burst neutrinos and covering more SN models with soft neutrino energy spectra. Here 10-50 MeV is a conservative option to demonstrate the sensitivity (detection probability) of the proposed supernova trigger at JinPing. Based on the energy spectrum in Equation 15, the selection efficiency of prompt energy cut is $\sim$88%. The other selection criteria are same as those in the nH analysis of Daya Bay θ_{13} measurement [18], which include a 3σ delayed energy cut for the 2.2-MeV gamma peak from neutron capture on H, a 1-400 μs prompt-delayed time coincidence cut, and a 500-mm prompt-delayed vertex distance cut. The product of the efficiencies of these selection criteria can be obtained from [18, 17]. As a result, the final selection efficiency of SN burst neutrinos is $\sim$50%. This selection efficiency will be considered in Equation 16 to correct the number of expected SN burst neutrinos when we calculate the detection probability of the supernova trigger (defined as the probability that a supernova neutrino burst will trigger or be detected).

Within a sliding 10-second window, the supernova trigger is determined from the IBD event distribution among detectors. As the background rate is estimated to be $<$1/yr based on our selection criteria, the expected number of backgrounds is rationally assumed to be ZERO within a 10-second window. Considering electronic noise or unexpected backgrounds, the supernova trigger is issued when $\geq$2 IBD signals are observed in one detector or two detectors within 10-second window. For two detectors, this trigger strategy means the case with no IBD signals or just 1 IBD signals in one of the two detectors will be ignored. The detection probability of the supernova trigger will be demonstrated below in two scenarios of one 1.5-kt liquid scintillator detector and two 1.5-kt liquid scintillator detectors.

With the expected number of SN burst neutrinos corrected with the selection efficiency and the trigger strategy mentioned above, assuming the number of events follows a Poisson distribution in one detector and different detectors are mutually independent, the detection probability is shown in Fig. 24 as a function of distance to the Earth. Notice that the most distance edge of the Milky Way is just 23.5 kpc from the Earth and SN 1987A exploded at a distance of 50 kpc. The larger distances will cover more SN explosions.

4.3 Discussions

From the description of the supernova trigger at JinPing above, the selection criteria of IBD events could be optimized for prompt energy cut and even other selection criteria due to the quite low background rate. Besides, the trigger strategy may be kind of conservative at present. Thus, the realistic detection probability of the supernova trigger at JinPing may be 100% throughout 100 kpc distance while the Fig. 24 shows a greater than 95% detection probability within 100 kpc in the scenario of two 1.5-kt detectors. Notice that the Super-K has 100% detection probability of the supernova neutrino bursts out to 100 kpc which is the same level as our proposed supernova trigger at JinPing. The total target mass is 3 kt to 22.5 kt.

Due to the deep rock cover, small detectors may only be allowed to distribute in JinPing. However, the coincidence detection from multiple detectors is robust against spatially uncorrelated backgrounds, which enables a better detection probability than a single detector. The experience

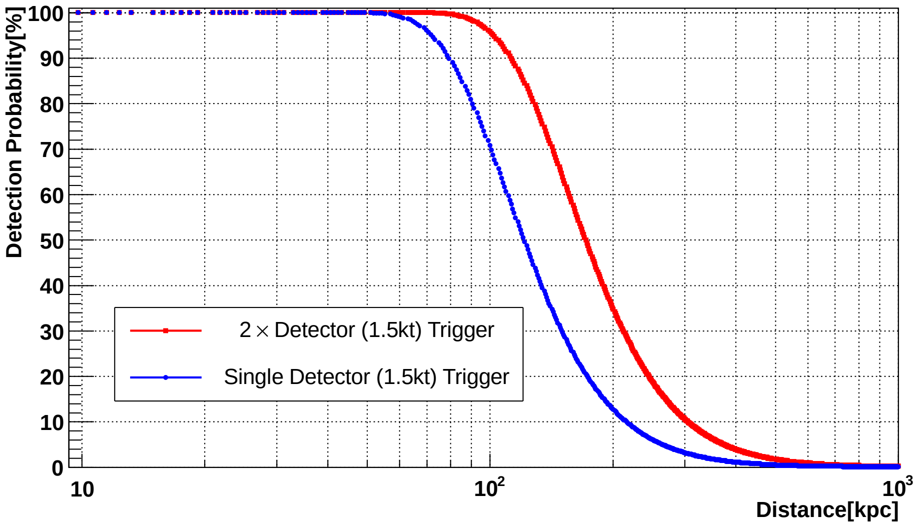

Figure 24: The red curve corresponds to two 1.5-kt liquid scintillator detectors and the blue curve corresponds to a 1.5-kt liquid scintillator detector.

and techniques can be referred to from the supernova trigger at Daya Bay [17].

Offline analysis of the supernova neutrino bursts will also benefit from the low background rate and multiple detectors to be spatially distributed. And a smaller total target mass may provide a quite good limit of the rate of supernova neutrino bursts with sufficient live time.

A water-based liquid scintillator [19] was in R&D recently in which scintillating organic molecules and water are co-mixed using surfactants. This WbLS study has made a great progress and the extensive development of the WbLS chemical cocktail is ongoing at BNL. The pure water detectors are primarily sensitive to high energy interactions creating particles above the Cherenkov threshold. The pure scintillator detectors (isotropy without directionality) are sensitive to low-energy events. With the WbLS, the pointing of the SN neutrino bursts may be achieved by identifying the direction of Cherenkov light from the neutrino-electron scattering interactions like Super-K which is the only experiment with pointing capability at present.

References

[1] K.S. Hirata, *et al.*, Phys. Rev. Lett. **58**, 1490 (1987).

[2] K.S. Hirata, *et al.*, Phys. Rev. D **38**, 448 (1988).

[3] R.M. Bionta, *et al.*, Phys. Rev. Lett. **58**, 1494 (1987).

[4] C.B. Bratton, *et al.*, Phys. Rev. D **37**, 3361 (1988).

[5] E.N. Alekseev, *et al.*, JETP Lett. **45**, 589 (1987).

[6] E.N. Alekseev, *et al.*, Phys. Lett. B **205**, 209 (1988).

[7] G.G. Raffelt, arXiv:1201.1637 (2012).

[8] R.N. Mohapatra and P.B. Pal, *Massive Neutrinos in Physics and Astrophysics*, World Scientific Publishing Co. Pte. Ltd. 2004.

[9] C. Lunardini and A.Y. Smirnov, JCAP **0306**, 009 (2003).

[10] P.D. Serpico, S. Chakraborty, T. Fischer, *et al.*, Phys. Rev. D **85**, 085031 (2012).

[11] C.D. Ott, E.P. O'Connor, S. Gossan, *et al.*, Nucl. Phys. B (Proc. Suppl.) **235-236**, 381 (2013).

[12] S. Ando, J.F. Beacom, H. Yüksel, Phys. Rev. Lett. **95**, 171101 (2005).

[13] SNEWS, *http://snews.bnl.gov (2015)*, *Supernova Early Warning System*

[14] K. Scholberg, *et al.*, New J. Phys. **6**, 114 (2004).

[15] G. Raffelt, I. Tamborra, B. Müller, L. Hüdepohl, H.T. Janka, Phys. Rev. D **86**, 125031 (2012).

[16] K. Scholberg, Annu. Rev. Nucl. Part. Sci. **62**, 81 (2012).

[17] Hanyu Wei, *et al.*, arXiv:1505.02501 (2015). arXiv:1505.02501 [astro-ph.IM].

[18] F.P. An, *et al.* (Daya Bay Collaboration), Phys. Rev. D **90**, 071101 (R) (2014).

[19] J. R. Alonso *et al.*, arXiv:1409.5864v3 (2014).

5 Geoneutrino

The study of geology by geoneutrino [1] was only practical recently by the advent of larger neutrino detectors [2, 3, 4, 5, 6]. The Earth heat flow was estimated as 46±3 TW. However controversial points were hold about the origin of this energy [7]. What fraction is from primordial or radioactive sources? This discussion is related to many profound questions of the Earth: the composition of the Earth, chemical layering in the mantle, mantle convection, the energy to drive Plate Tectonics, and the power source of the geodynamo. Jinping is far away from all currently running or planned reactors and the coast line of China, so the dominant reactor neutrino background is rather low and it will make a conclusive measurement of crust geoneutrino flux of the Earth.

5.1 Reactor antineutrino background

Reactor antineutrino background is the major background to the search of geoneutrinos. It cannot be eliminated by material purification or carrying out an experiment in deep underground. However, Jinping is much further to reactors than all other neutrino experiments, such as Borexino and SNO underground experiments, which makes Jinping an ideal site for such a study. Next we will estimate in detail the reactor antineutrino background rate at Jinping.

5.1.1 Differential neutrino flux of a single reactor

Reactor antineutrinos are primarily from the beta decays of four main fissile nuclei ^{235}U, ^{238}U, ^{239}Pu, and ^{241}Pu. The differential $\bar{\nu}_e$ flux, $\phi(E_\nu)$, for a reactor is estimated as

$$\phi(E_\nu) = \frac{W_{th}}{\sum_i f_i e_i} \sum_i f_i S_i(E_\nu), \tag{17}$$

where i sums over the four isotopes, W_{th} is the thermal power of a reactor which can be found in IAEA [9], f_i ($\sum_i f_i = 1$) is the fission fraction of each isotope, e_i is the average energy released per fission of each isotope, and $S_i(E_\nu)$ is the antineutrino spectrum per fission of each isotope. A set of typical fission fractions, f_i, and the average energy released per fission, e_i, are listed in Tab. 7. The spectrum of each isotope, $S_i(E_\nu)$, and their sum are shown in Fig. 25.

Isotope	f_i	e_i [MeV/fission]
^{235}U	0.58	202.36 ± 0.26
^{238}U	0.07	205.99 ± 0.52
^{239}Pu	0.30	211.12 ± 0.34
^{241}Pu	0.05	214.26 ± 0.33

Table 7: Fission fraction and average released energy of each isotope.

5.1.2 Total differential reactor neutrino flux

To get the total reactor neutrino background spectrum at Jinping, $\phi_{Jinping}(E_\nu)$, the thermal powers of all currently running and under construction reactors are extracted from IAEA [9], and the electron antineutrino survival probability is also taken into account. $\phi_{Jinping}(E_\nu)$ is expressed as

$$\phi_{Jinping}(E_\nu) = \sum_i^{Reactors} \phi_i(E_\nu) P_{\bar{\nu}_e \to \bar{\nu}_e}(E_\nu, L) \frac{1}{4\pi L^2}, \tag{18}$$

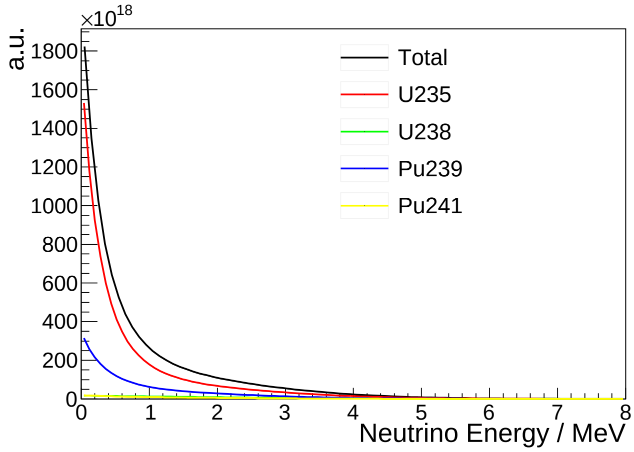

Figure 25: Reactor antineutrino spectrum for each isotope and their sum.

with

$$P_{\bar{\nu}_e\to\bar{\nu}_e}(E_\nu, L) \approx 1 - \sin^2 2\theta_{12} \sin^2\left(1.267\frac{\Delta M^2_{21}(\mathrm{eV})L(\mathrm{km})}{E_\nu(\mathrm{GeV})}\right), \tag{19}$$

where E_ν is the neutrino energy, L is the distance from each reactor to Jinping site, and θ_{12} and ΔM^2_{21} are neutrino oscillation parameters. L is estimated using the longitude and latitude of each reactor and Jinping site, and θ_{12} and ΔM^2_{21} are set to be 0.586 and 7.58×10^{-5} eV^2, respectively. The total differential spectrum at Jinping of all reactors constructed or under contruction is shown in Fig. 26 and the total flux is summarized in Tab. 8.

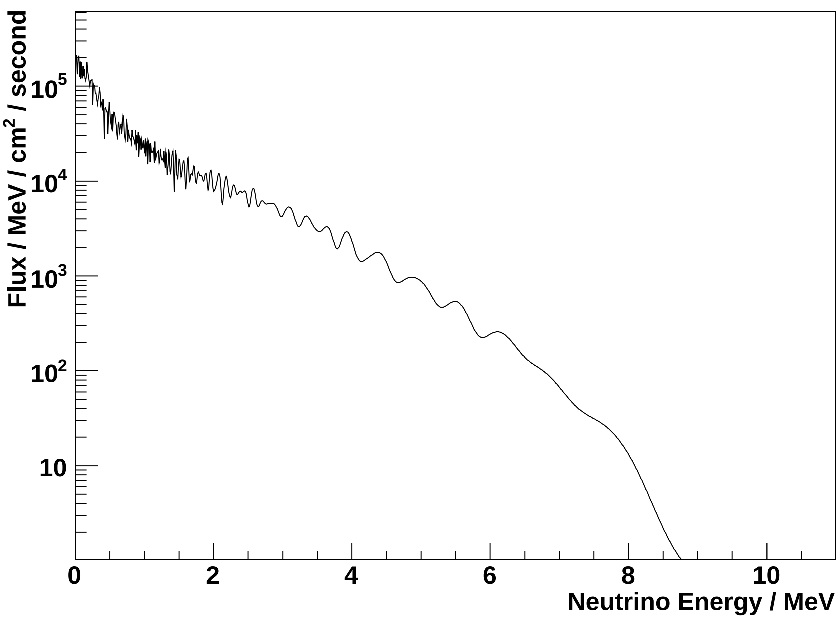

Figure 26: Total differential reactor neutrino flux at Jinping.

5.1.3 Total reactor neutrino event rate

Electron antineutrinos will be primarily detected by inverse beta decay (IBD) process, $\bar{\nu}_e + p \to e^+ + n$. The reaction has a threshold of 1.8 MeV and what we measured, E_{vis}, is the positron kinetic energy plus the energy of two 0.511 MeV gammas,

$$E_{vis} = E_\nu - 0.78 \text{ MeV}. \tag{20}$$

With the total differential flux including all future reactors calculated above and the cross section of IBD, $\sigma(E_\nu)$ [8], the rate of detectable events can be calculated as

$$R_{Jinping}(E_\nu) = \phi_{Jinping}(E_\nu) \times \sigma(E_\nu). \tag{21}$$

With a modest setup, for example, 1 kiloton detector and 1500 days' data-taking, the differential rate spectrum is shown in Fig. 27, where we assumed the number of free protons fraction is 12% and the total event rate is summarized in Tab. 9.

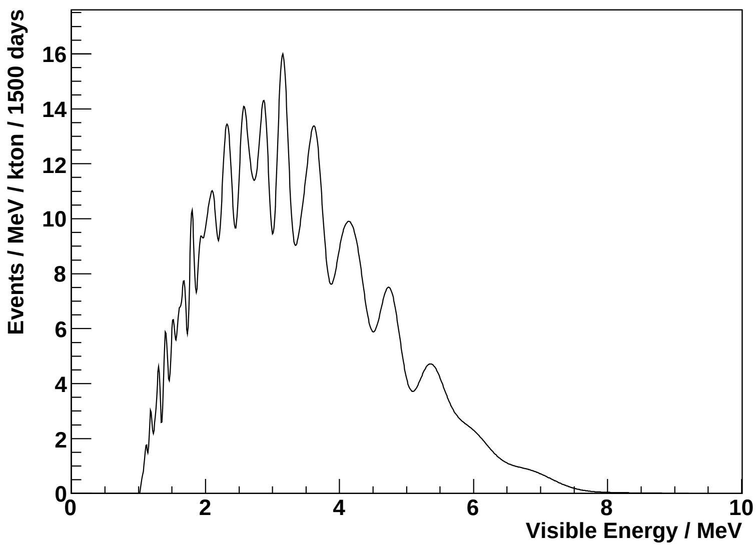

Figure 27: Reactor neutrino energy spectrum in Jinping.

5.2 Geoneutrino spectrum and flux

We adopt the geo-neutrino spectrum in [10]. The visible energy spectrum of geoneutrinos is shown in Fig. 28 overlapped with the reactor background estimated previously. Geoneutrinos can be clearly identified.

JinPing	Constructed		Under Construction		Total
	China	Others	China	Others	
$\phi_\nu/(10^5\text{cm}^2\text{s})$	2.412	1.687	3.956	0.226	8.281

Table 8: Reactor neutrino flux at JinPing.

JinPing	Constructed		Under Construction		Total
	China	Others	China	Others	
Rate/kton/1500day	11.7	8.2	19.2	1.1	40.2

Table 9: Reactor neutrino event rate at JinPing.

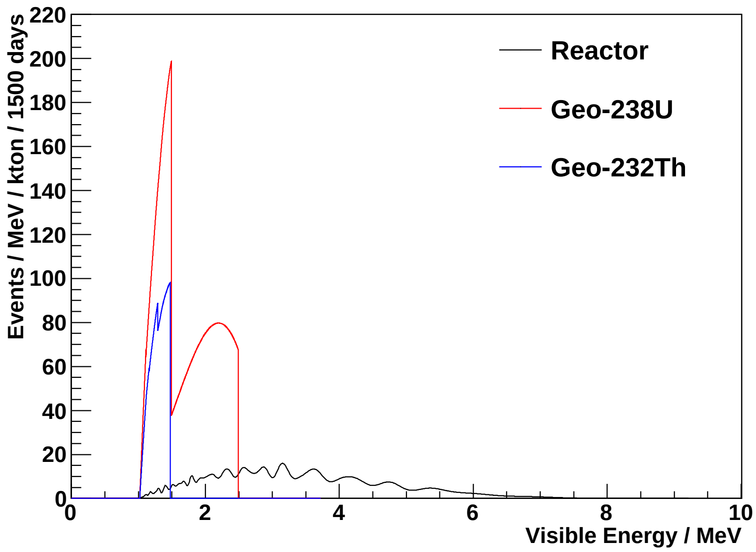

Figure 28: Geoneutrino and reactor neutrino spectra at Jinping.

5.3 Sensitivity at Jinping

Jinping is far away from all currently running and being constructed reactors. Fig. 28 clearly shows that reactor neutrino background becomes insignificant and a precise geoneutrino flux measurement will be avaiable, especially for the component from the crust of the Earth. Jinping is an ideal site to search geoneutrinos.

References

[1] William F. McDonough and Ondřej *Šrámek*, Environ. Earth Sci. **71**, 3787 (2014).

[2] T. Araki, *et. al.* (KamLAND Collaboration), Nature **436**, 499 (2005).

[3] A. Gando, *et. al.* (KamLAND Collaboration), Nature Geoscience **4**, 647 (2011).

[4] A. Gando, *et. al.* (KamLAND Collaboration), arXiv:1303.4667 (2013).

[5] G. Bellini, *et. al.* (Borexino Collaboration), Phys. Lett. **B 687**, 299 (2010).

[6] G. Bellini, *et. al.* (Borexino Collaboration), Phys. Lett. **B 722**, 295 (2013).

[7] G. Bellini, *et. al.*, Prog. Part. Nucl. Phys. **73**, 1 (2013).

[8] P. Vogel and J. F. Beacom, Phys. Rev. D 60 053003 (1999).

[9] International Atomic Energy Agency, http://www.iaea.org/ (2015).

[10] S. Enomoto, Neutrino geophysics and observation of geo-neutrinos at KamLAND, Ph.D. Thesis, Tohoku University (2005).

6 Atmospheric neutrino

Atmospheric neutrino is a natural resource that can be used to measure the neutrino mass hierarchy, the octant of the atmospheric mixing angle θ_{23}, and the Dirac CP phase δ. In contrast to fixed baseline experiments, atmospheric neutrinos can experience baseline lengths ranging from 10 km, which is the typical height of atmosphere, to around 12600 km, which is the Earth diameter. The neutrino energy also spans a wide range from $\mathcal{O}(MeV)$ to very high energy. This gives it benefits of exploring various oscillation frequencies.

With the reactor angle θ_{13} being measured by reactor neutrino experiments Daya Bay and RENO, three mixing parameters (the neutrino mass hierarchy, the CP phase δ, and the atmospheric mixing angle θ_{23}) need to be further measured. Atmospheric neutrino oscillations can try to measure all three of them.

According to the Preliminary Reference Earth Model (PREM) [1], the earth can be mainly divided into two layers, the mantle and the core with the latter further divided into the outer core and the inner core. The matter density is quite different for different layers and keeps increasing when going deeper into the Earth, as shown in Fig. 29. For neutrinos going along different baselines, not only the baseline length is different, but also the matter density that neutrinos experience. Atmospheric neutrinos have very rich features for studying neutrino oscillations.

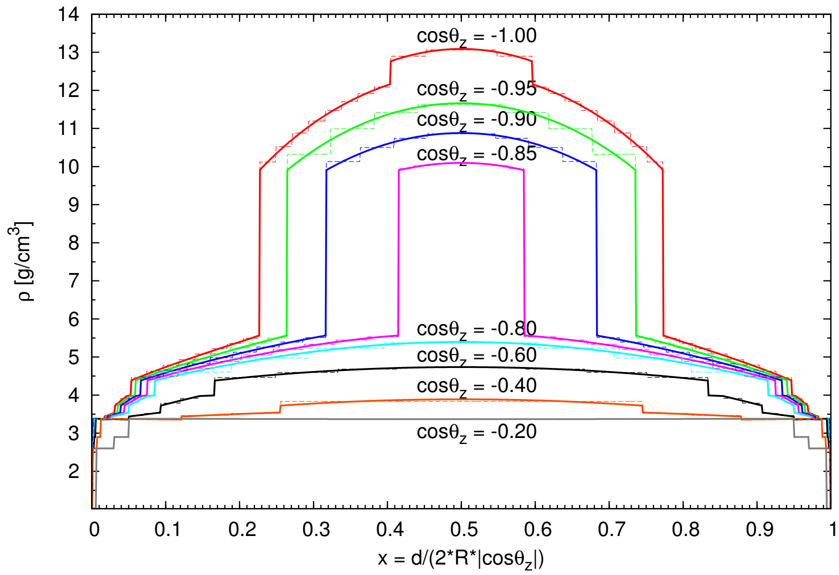

Figure 29: PREM matter density profile along neutrino trajectories [2].

6.1 Low energy atmospheric neutrinos

The atmospheric neutrinos are produced from decay of pion and muon which are in turn products of cosmic ray interactions in the Earth atmosphere. Once produced, pion and muon fly through air before decay. At low energy, $E_\nu < 100$ MeV, pion and muon can decay either in motion or at rest. This leads to distinctive features in the resulting neutrino flux [3] as shown in Fig. 30.

The electron (anti-)neutrino fluxes are quite different from the muon (anti-)neutrino fluxes. This is because the former is continuous in the whole energy range while the latter has discontinuity at the neutrino energy spectrum end-point from μDAR, E^μ_ν, and a peak around the end-point from πDAR.

Once produced, pion loses energy during propagation and then decays at rest (πDAR) with two final-state particles, $\pi \to \mu + \nu_\mu$, which are monochromatic. If all pions decay at rest, this property of being monochromatic leads to a δ-function peak. This does not happen since pion has chances to decay before being fully stopped. Together, the neutrinos from pion decay form a peak around E^π_μ. On the other hand, muon decay has three final-state particles, $\mu \to e + \nu_\mu + \nu_e$. The spectrum of ν_μ keeps rising until hitting the spectrum end-point $E^\mu_\nu \approx 53$ GeV while that of ν_e has a peak around 35 GeV and decreases to zero

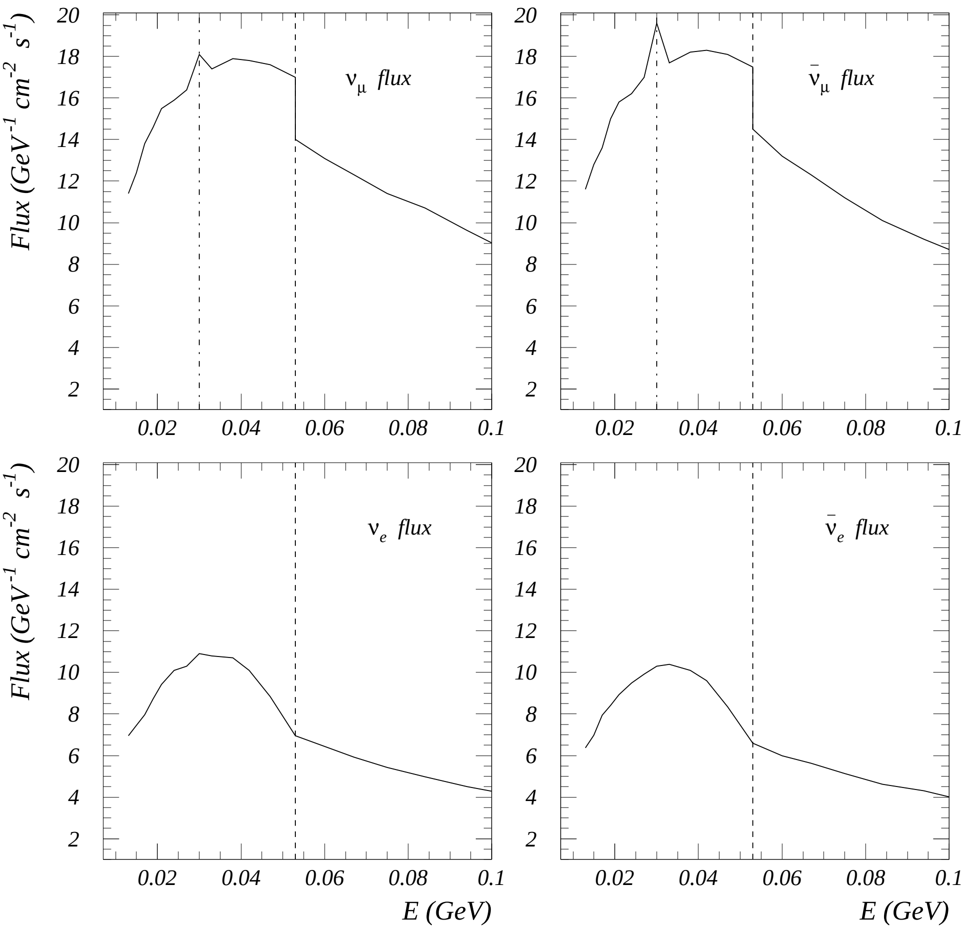

Figure 30: The fluxes of ν_μ, $\bar{\nu}_\mu$, ν_e, and $\bar{\nu}_e$ neutrinos as functions of neutrino energy [4]. The dashed vertical lines show the end-point of the neutrino energy spectrum from the muon decay at rest (μDAR), $E^\mu_\nu \approx 53$ GeV, and the neutrino energy from the pion decay at rest (πDAR), E^π_ν.

when approaching E^μ_ν, leading to discontinuity in the ν_μ spectrum and continuous ν_e spectrum as shown in Fig. 31.

The low energy atmospheric neutrino oscillation can be used to constrain the atmospheric mixing angle θ_{23} and the CP phase δ [4]. The electron-like events changes by $15 \sim 20\%$ the variation of θ_{23} and roughly 10% by the variation of δ.

When detecting neutrino interaction events, it is usually difficult to reconstruct the neutrino energy. For CCQE, the electron energy is roughly the neutrino energy and hence can be used to give a good estimation of the neutrino energy. But for resonance, electron can only take away a fraction of the neutrino energy. If these two types of events cannot be distinguished, neutrinos from higher energy can produce electron with energy at lower energy and become background. Another possible background comes from μDAR produced by the atmospheric muon neutrinos.

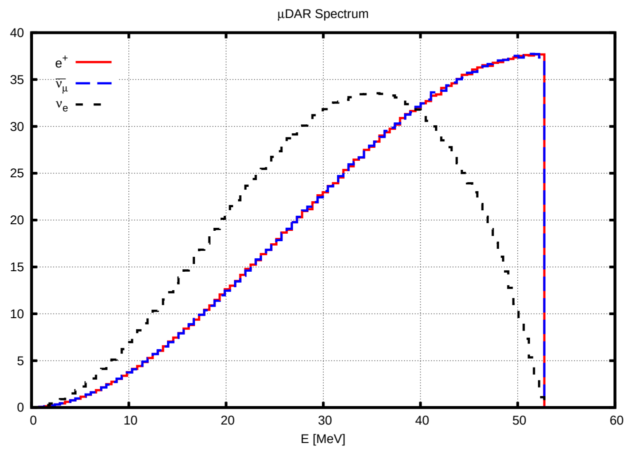

Figure 31: Muon decay at rest (μDAR) spectrum.

6.2 Sub-GeV atmospheric neutrinos

At lower energy the effect of the Dirac CP phase in neutrino mixing is more apparent. It is possible to use low energy atmospheric neutrinos to measure this unknown CP phase. A 20kton scintillator detector at the Jinping site can provide more than 1σ sensitivity with 10 years of running.

In the low energy region $E_\nu < 0.5$GeV, the oscillation probability is modulated by both Δm^2_{12} (envelope) and Δm^2_{13} (high frequency oscillation part) as shown in Fig. 32.

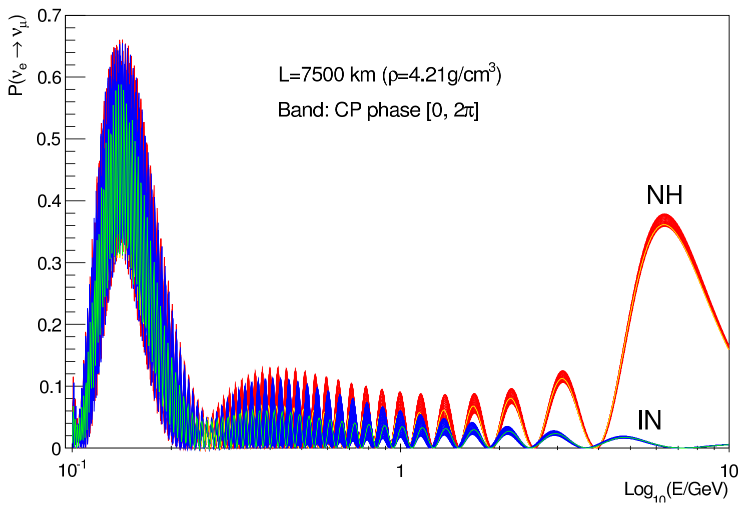

Figure 32: The dependence of the oscillation probability $P(\nu_e \to \nu_\mu)$ on the Dirac CP phase δ at $L = 7500$km and matter density $\rho = 4.21\text{g/cm}^3$ for the normal (red) and inverted (blue) mass hierarchy. The band is the variation with $\delta \sim [0, 2\pi]$ and yellow line or green line corresponds to $\delta = 0$ curve in it.

To show the dependence on the Dirac CP phase δ, we adopt the decomposition formalism in the propagation basis [2],

$$P_{\alpha\beta} \equiv P^{(0)}_{\alpha\beta} + P^{(1)}_{\alpha\beta} x_{\rm a} + P^{(2)}_{\alpha\beta} \cos\delta'_D + P^{(3)}_{\alpha\beta} \sin\delta'_D + P^{(4)}_{\alpha\beta} x_{\rm a} \cos\delta'_D + P^{(5)}_{\alpha\beta} x^2_{\rm a} + P^{(6)}_{\alpha\beta} \cos^2\delta'_D\,, \quad (6.1a)$$

$$\overline{P}_{\alpha\beta} \equiv \overline{P}^{(0)}_{\alpha\beta} + \overline{P}^{(1)}_{\alpha\beta} x_{\rm a} + \overline{P}^{(2)}_{\alpha\beta} \cos\delta'_D + \overline{P}^{(3)}_{\alpha\beta} \sin\delta'_D + \overline{P}^{(4)}_{\alpha\beta} x_{\rm a} \cos\delta'_D + \overline{P}^{(5)}_{\alpha\beta} x^2_{\rm a} + \overline{P}^{(6)}_{\alpha\beta} \cos^2\delta'_D\,, \quad (6.1b)$$

for neutrino and anti-neutrino, respectively. The expansion parameter x_a is defined as the deviation of the atmospheric mixing angle $\theta_a(\equiv \theta_{23})$ away from its maximal value,

$$x_a \equiv \cos 2\theta_a \,, \tag{6.2}$$

while the cosine and sine functions of δ has been modulated by a common factor,

$$\cos\delta'_D \equiv 2c_{\rm a}s_{\rm a}\cos\delta \approx \sqrt{1-x_{\rm a}^2}\cos\delta\,, \qquad \sin\delta'_D \equiv 2c_{\rm a}s_{\rm a}\sin\delta \approx \sqrt{1-x_{\rm a}^2}\sin\delta\,. \tag{6.3}$$

For completeness, we show all the expansion coefficients in (6.4).

	$P^{(k)}_{\rm ee}$	$P^{(k)}_{{\rm e}\mu}$	$P^{(k)}_{\mu{\rm e}}$	$P^{(k)}_{\mu\mu}$
(0)	$\lvert S'_{11}\rvert^2$	$\frac{1}{2}(1-\lvert S'_{11}\rvert^2)$	$\frac{1}{2}(1-\lvert S'_{11}\rvert^2)$	$\frac{1}{4}\lvert S'_{22}+S'_{33}\rvert^2$
(1)	0	$\frac{1}{2}(\lvert S'_{12}\rvert^2-\lvert S'_{13}\rvert^2)$	$\frac{1}{2}(\lvert S'_{12}\rvert^2-\lvert S'_{13}\rvert^2)$	$\frac{1}{2}(\lvert S'_{22}\rvert^2-\lvert S'_{33}\rvert^2)$
(2)	0	$\mathbb{R}(S'_{12}S'^{*}_{13})$	$\mathbb{R}(S'_{12}S'^{*}_{13})$	$-\mathbb{R}(S'_{12}S'^{*}_{13})$
(3)	0	$\mathbb{I}(S'_{12}S'^{*}_{13})$	$-\mathbb{I}(S'_{12}S'^{*}_{13})$	0
(4)	0	0	0	$\mathbb{R}[S'_{23}(S'_{22}-S'_{33})^*]$
(5)	0	0	0	$\frac{1}{4}\lvert S'_{22}-S'_{33}\rvert^2$
(6)	0	0	0	$\lvert S'_{23}\rvert^2$

(6.4)

The dependence on the Dirac CP phase δ enters via $P^{(2)}$, $P^{(3)}$, $P^{(4)}$, and $P^{(6)}$. Nevertheless, the contribution from $P^{(4)}$ is suppressed by the associated expansion parameter x_a while $P^{(6)}$ is small due to hierarchical structure between the two mass square differences, $\Delta m^2_{12}/\Delta m^2_{13} \approx 3\%$. Consequently, it is enough to consider the two coefficients $\mathbb{R}(S'_{12}S'^{*}_{13})$ and $\mathbb{I}(S'_{12}S'^{*}_{13})$. Note that, these amplitude matrix elements S'_{ij} are obtained in the propagation basis. They are functions of neutrino energy and zenith angle.

At low energy, the detector resolution is not good enough to recognize all the fast oscillations as shown in Fig. 32. To see the signal distribution after smearing, we implement Fast Fourier Transform (FFT) to the energy dependence of the decomposition coefficients. The results are shown in Fig. 33. After filtering

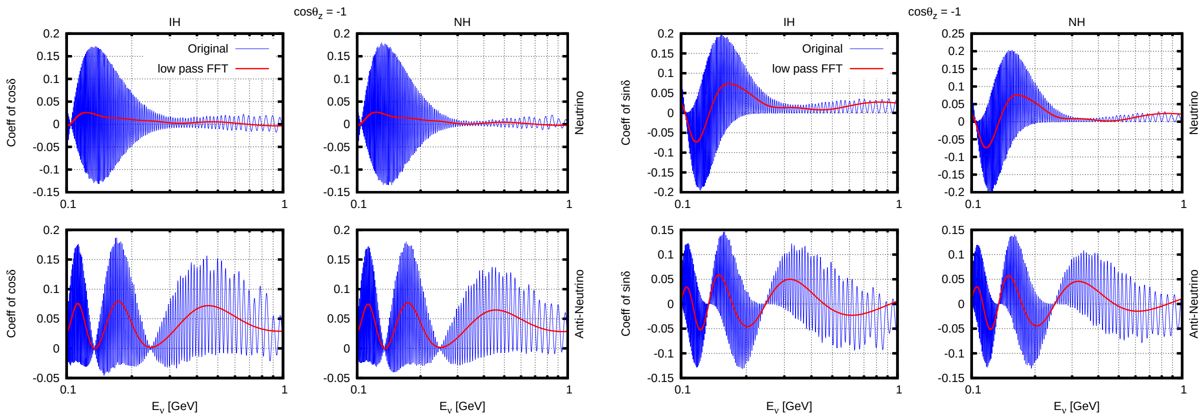

Figure 33: Coefficients $P^{(2)} = \mathbb{R}(S'_{12}S'^{*}_{13})$ of $\cos\delta$ (left) and $P^{(3)} = \mathbb{I}(S'_{12}S'^{*}_{13})$ of $\sin\delta$ (right), respectively, for neutrinos traveling through the Earth center ($\cos\theta_z = -1$). In each of the two panels, the left column is for IH with the right for NH, while the first row is for neutrino and the second for anti-neutrino. Within each subplot, the blue curves are the original one while the red is the one surviving the low-pass FFT.

out the high-frequency oscillation modulated by Δm^2_{13}, the low-frequency part modulated by Δm^2_{12} is still sizable. Across the Sub-GeV range, the effect of the Dirac CP phase δ on the oscillation probability can be as large as 7%. This indicates the size of the effect that the Dirac CP phase can generate.

From the point of view of detection capability, the region above 100MeV has less fast neutrons induced by muons for tagging. In addition, the atmospheric neutrino flux is not precisely constrained below 100MeV, and hence would introduce large systematic error. On the other hand, the region above 300MeV has no pion production in CC process and the atmospheric neutrino flux is low there. These factors determine the energy region selected in our study to be between 100MeV and 300MeV.

However, in this energy range, the correlation of the lepton direction with its initial neutrino direction is rather weak, thus the direction information is totally discarded in practice. After integration over the zenith angle, the energy information may also get lost to some extend and just one energy bin covering $100 \sim 300$MeV is used for analysis.

The event number is a convolution of the atmospheric flux, oscillation probability, exposure time and cross sections,

$$\begin{aligned} \text{Number of signal } [1/(\text{kt} \cdot \text{year})] \; = \; & \text{Flux(E, zenith, v-flavor) } [1/(\text{GeV} \cdot \text{sr} \cdot s \cdot \text{m}^2)] \\ & \times 2\pi \cdot d\text{cos(zenith) [sr]} \times d\text{E [GeV]} \\ & \times \text{Oscillation-Probability(zenith, v-flavor, } \delta_{CP}\text{, Mass-Hierarchy)} \\ & \times \text{Exposure } [60{\cdot}60{\cdot}24{\cdot}365 \text{ s/year}] \\ & \times \Sigma\{\sigma(\text{nucleus, E, v-flavor) } [\text{m}^2] \cdot \text{N(nuclei) [/kt]}\}. \end{aligned}$$

Before using χ^2 fit to do the analysis, let us first take a look at the contribution from different flavors. Here we just show the discrepancy between $\delta_{CP} = 0$ and $\delta_{CP} = 0.7\pi$ which is defined as $\frac{N(\delta_{CP}=0)-N(\delta_{CP}=0.7\pi)}{N(\delta_{CP}=0)+N(\delta_{CP}=0.7\pi)}$ where N is the integrated number of signal in the 100$\sim$300 MeV region over all directions. Tab. 10 shows the discrepancies for all the cases with various initial neutrino flux of one flavor to some final neutrino flavor and the number of signal with exposure time 200 kt·year, $\delta_{CP} = 0$ is also listed in the bracket to show the statistical difference.

initial \ final	$\bar{\nu}_e$	$\bar{\nu}_\mu$	ν_e	ν_μ
$\bar{\nu}_e$	×(413)	25%(30)	–	–
$\bar{\nu}_\mu$	10%(111)	-3%(356)	–	–
ν_e	–	–	×(860)	-11.5%(94)
ν_μ	–	–	-2.6%(317)	2.4%(808)

Table 10: Summary of the discrepancies (see the text for the definition here) between $\delta_{CP} = 0$ and $\delta_{CP} = 0.7\pi$ for various neutrino oscillation channels. The '×' means no CP sensitivity and '–' means forbidden oscillation channel.

Since the CP phase does not appear in the electron flavor to electron flavor transitions, there is no contribution from $\nu_e \to \nu_e$ or $\bar{\nu}_e \to \bar{\nu}_e$. For ν_μ or $\bar{\nu}_\mu$ final state, the two contributions have opposite signs, leading to unavoidable cancellation.

To study the significance exactly, we adopt χ^2 fit with Possion distribution,

$$L(N^{exp}, N^{obs}) = \prod_{i=1}^{n} \frac{(N_i^{exp})^{N_i^{obs}} \cdot e^{-N_i^{exp}}}{N_i^{obs}!} \,, \tag{6.5}$$

for n bins. Since only one bin is utilized in our analysis, the summation can be omitted. The corresponding χ^2 function is given by the log-likelihood ratio,

$$\chi^2 = -2 \ln \frac{L(N^{exp}, N^{obs})}{L(N^{obs}, N^{obs})} = 2(N^{exp} - N^{obs} + N^{obs} \ln \frac{N^{obs}}{N^{exp}}). \tag{6.6}$$

Here define $\chi^2(0)$ to represent the χ^2 with N^{obs} conditioning $\delta_{CP} = 0$ and $\chi^2(\pi)$ to represent that conditioning $\delta_{CP} = \pi$. The significance level of the CP violation discovery sensitivity is $\sqrt{\Delta\chi^2}$, where

$$\Delta\chi^2 = \min\{\chi^2(0), \chi^2(\pi)\}. \tag{6.7}$$

So each δ_{CP} value corresponds to a significance level, in which case the N^{exp} is the number of signal varying with the corresponding δ_{CP} value.

We have computed the sensitivity results based on a 20 kt $\times$ 10 year = 200 kt·year liquid scintillator detector. The various scenarios including ν_μ plus $\bar{\nu}_\mu$ detection combined result, ν_e plus $\bar{\nu}_e$ detection combined result and all channels detection combined result. Here we assume the flavor of the detected neutrino is available and no systematic uncertainty involved. The oscillation parameters of the PMNS matrix are also fixed without marginalization. The sensitivity results shown in the last section implies 1σ significance level of sensitivity at some δ_{CP} range.

Fig. 34 shows the results for various scenarios. The plot (a) in Fig. 34 demonstrates the sensitivity result for electron (anti) neutrino detection in which case the ν_μ (merged with ν_e) to ν_e channel and $\bar{\nu}_\mu$ (merged with $\bar{\nu}_e$) to $\bar{\nu}_e$ channel are combined. The initial flavor of the neutrino is impossible to know but the final flavor is assumed to be distinguishable. Similarly, the plot (b) in Fig. 34 demonstrates the sensitivity result for muon (anti) neutrino detection.

The scale of plot (a) is larger than plot (b) mainly due to the counteractive merge for case (b) of the δ_{CP} effect on the events of ν_e ($\bar{\nu}_e$) to ν_μ ($\bar{\nu}_\mu$) and ν_μ ($\bar{\nu}_\mu$) to ν_μ ($\bar{\nu}_\mu$) which can be seen in Tab. 10. But the patterns of (a) and (b) curves are different due to the oscillation probability dependence on δ_{CP}. The electron (anti) neutrino detection result contains ν_e ($\bar{\nu}_e$) to ν_e ($\bar{\nu}_e$) oscillation which is independent of δ_{CP} and ν_μ ($\bar{\nu}_\mu$) to ν_e ($\bar{\nu}_e$) oscillation which is approximately dependent on $cos(\Delta + \delta_{CP})$ plus δ_{CP} unrelated terms. The Δ here is related to L/E and Δm^2 and would introduce a special point $\delta_{CP} = 2(\pi - \Delta)$ in which case CP violation sensitivity vanishes. From the above, the plot (a) shows a periodic pattern of the sensitivity curve against the δ_{CP} with the cycle of π. But the muon (anti) neutrino detection result is different with the electron neutrino result due to the channel ν_μ ($\bar{\nu}_\mu$) to ν_μ ($\bar{\nu}_\mu$) oscillation dependence on δ_{CP}. This dependence shows a symmetry about $\delta_{CP} = \pi$ and would break the periodic pattern like plot (a) resulting plot (b). Please notice that the result shown is the integral result of the oscillation in matter based on a large range of L/E weighted by the flux and cross section. The plot (c) in Fig. 34 is the final result considering all the channels which is actually the combination of (a) and (b).

6.3 Multi-GeV atmospheric neutrinos

With energy in the multi-GeV range, neutrino can experience resonances when crossing the Earth, which happens for neutrino if the mass hierarchy is normal or for anti-neutrino if inverted. Because of this, the difference between neutrino and anti-neutrino oscillation probabilities can be maximal. Hence a magnetized experiment with ability of distinguishing neutrino from anti-neutrino has the advantage of measuring the neutrino mass hierarchy. In addition, the mass hierarchy sensitivity is almost independent of the CP phase, in contrast to the accelerator based neutrino experiments which have degeneracy. The other thing that can be measured by atmospheric neutrino oscillation experiment is the atmospheric mixing angle θ_{23}.

6.3.1 Oscillation Features

For multi-GeV neutrino, its propagation through the Earth mantle and core can be significantly affected by matter potential which is roughly,

$$V = \pm\sqrt{2}G_F N_e \approx \pm\frac{|\delta m_a^2|}{2E_\nu}\,, \tag{6.8}$$

where $+$ is for neutrino and $-$ for anti-neutrino. For convenience, we define $\delta m_a^2 \equiv \delta m_{13}^2$. The effective mixing angle $\tilde{\theta}_r$ can be approximately expressed as,

$$\sin 2\tilde{\theta}_r \approx \frac{\sin 2\theta_r}{\sqrt{\sin^2 2\theta_r + \left(\cos 2\theta_r - \frac{2E_\nu V}{\delta m_a^2}\right)^2}}\,, \tag{6.9}$$

with $\theta_r \equiv \theta_{13}$ since it was measured by reactor neutrino experiments Daya Bay and RENO. If the neutrino mass hierarchy is normal, $\delta m_a^2 > 0$, the effective mixing angle $\tilde{\theta}_r$ is amplified to be maximal for neutrino. This is the so-called MSW resonance [5, 6, 7, 8]. The same thing happens for anti-neutrino, if the neutrino mass hierarchy is inverted. This feature can serve as a direct signal of the neutrino mass hierarchy. The

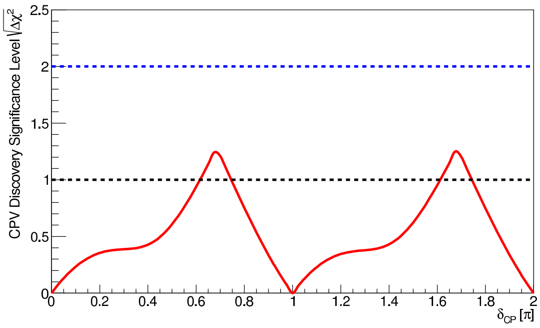

(a) ν_e plus $\bar{\nu}_e$

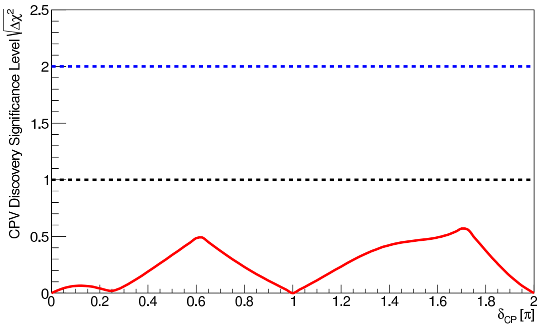

(b) ν_μ plus $\bar{\nu}_\mu$

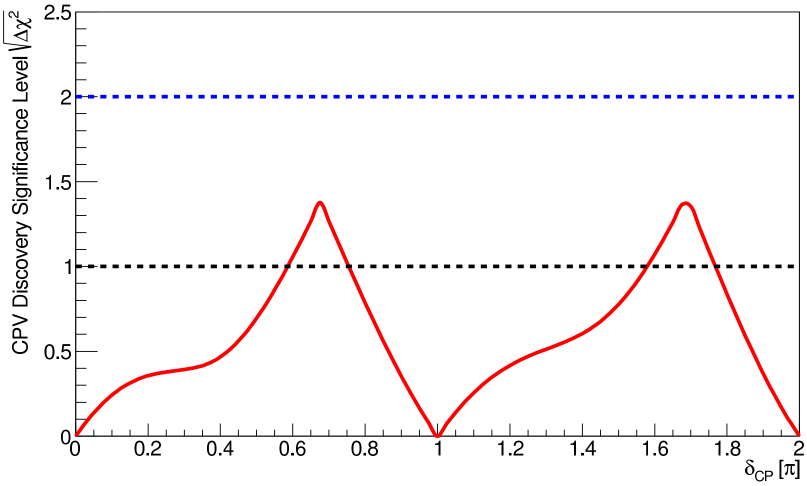

(c) All channels, combine (a) and (b)

Figure 34: The CP violation discovery (sensitivity) significance level for various scenarios.

most sensitive region is around $4 \sim 5$ GeV as shown in Fig. 35. Due to resonance, neutrino oscillogram has much richer structure if the neutrino mass hierarchy is normal. For inverted hierarchy $P_{ee} \approx 1$ in the whole region.

Nevertheless, both neutrino and anti-neutrino are present in the atmospheric neutrino flux. If they have the same flux, the total flux is insensitive to mass hierarchy since MSW resonance can happen for either neutrino or anti-neutrino, no matter which mass hierarchy is true. Fortunately, the neutrino flux is larger than the anti-neutrino flux. So there is some residual sensitivity for charge blind detectors such as PINGU. This can be further enhanced by using inelasticity to statistically distinguish between neutrino and anti-neutrino or building a detector with ability of doing this event by event which is even better. One candidate is INO [9] and we will discuss the advantage of doing this in the Jinping underground laboratory.

6.3.2 Detector and Reconstruction

The basic idea of telling neutrino from anti-neutrino is using magnetic field to see if the primary lepton from neutrino interaction is positively or negatively charged. This technique is most suitable for $\mu^\pm$ since it has long life time and can penetrate the calorimeter leaving a long track. Under the influence of strong magnetic field, the tracks bends to opposite directions for $\mu^\pm$. The charge recognition efficiency $\epsilon^\pm_{CID}$ for $\mu^\pm$ is a function of the muon energy E_μ. If E_μ is too small, the muon length is too short to be reconstructed

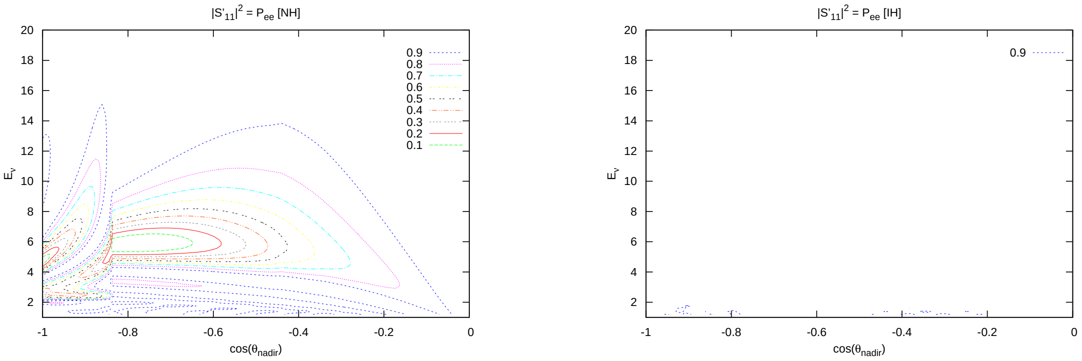

Figure 35: Atmospheric neutrino oscillogram for P_{ee} [2].

precisely. On the other hand, the bending curvature would be too small to tell the sign of charge for sure if E_μ is too large. In addition, ϵ^μ_{CID} is also a function of the muon zenith angle. This is because the detector is constructed as a stack of iron plates horizontally. For muons moving vertically, it goes the iron plates head-on and its track is recorded with more hits. On the other hand, for muons moving horizontally, it goes through less layers of iron plates and hence less hits is recorded. The result from INO simulation [9] has been shown in Fig. 36. The final event rate is subject to both reconstruction and charge identification efficiencies,

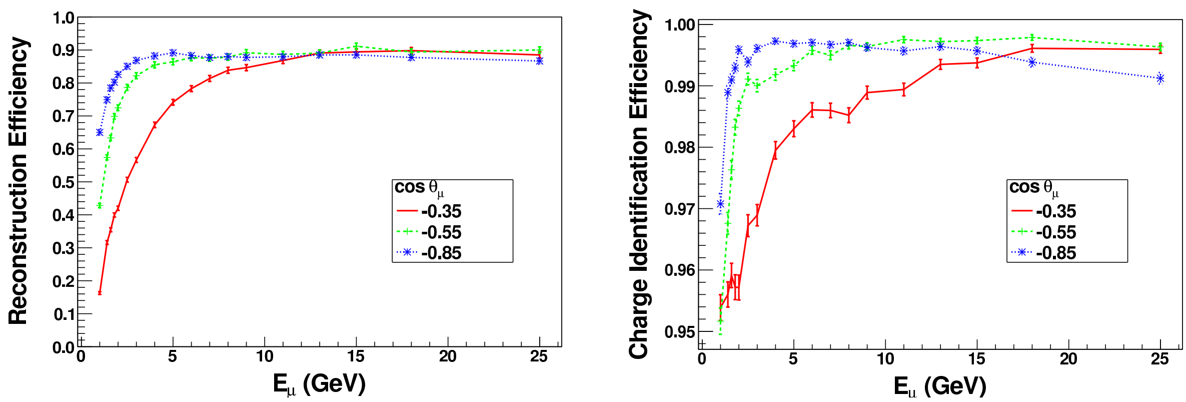

Figure 36: Muon reconstruction and charge identification efficiencies ϵ_R (left) and ϵ_{CID} (right) [9].

$$\begin{aligned} N_{\mu^\pm}(E_\mu, \cos\theta_\mu) &= \epsilon^\pm_{CID}(E_\mu, |\cos\theta_\mu|)\epsilon^\pm_R(E_\mu, |\cos\theta_\mu|) \times N^{true}_{\mu^\pm}(E_\mu, \cos\theta_\mu) \\ &+ [1 - \epsilon^\mp_{CID}(E_\mu, |\cos\theta_\mu|)]\epsilon^\mp_R(E_\mu, |\cos\theta_\mu|) \times N^{true}_{\mu^\mp}(E_\mu, \cos\theta_\mu)\,. \end{aligned} \tag{6.10}$$

Note that the zenith angle dependence is through $|\cos\theta_\mu|$. This because the iron layers are placed horizontally and has symmetric geometry around $\cos\theta_\mu = 0$. Since the sign of charge is not an essential factor for reconstruction and charge identification efficiencies, it is a reasonable assumption that,

$$\epsilon_R = \epsilon^\pm_R\,, \qquad \epsilon_{CID} = \epsilon^\pm_{CID}\,. \tag{6.11}$$

The Fig. 36 shows the energy dependence of ϵ_R and ϵ_{CID}. We can see that above 5GeV, muon reconstruction and charge identification are quite good. Below 5GeV, the situation becomes worth. Nevertheless, the charge identification is still good enough. The really observed event rates can be obtained by smearing (6.10) by energy and zenith angle resolution functions whose energy dependence has been plotted in Fig. 37. We can see that the zenith angle resolution decreases with energy while the energy resolution first decreases and

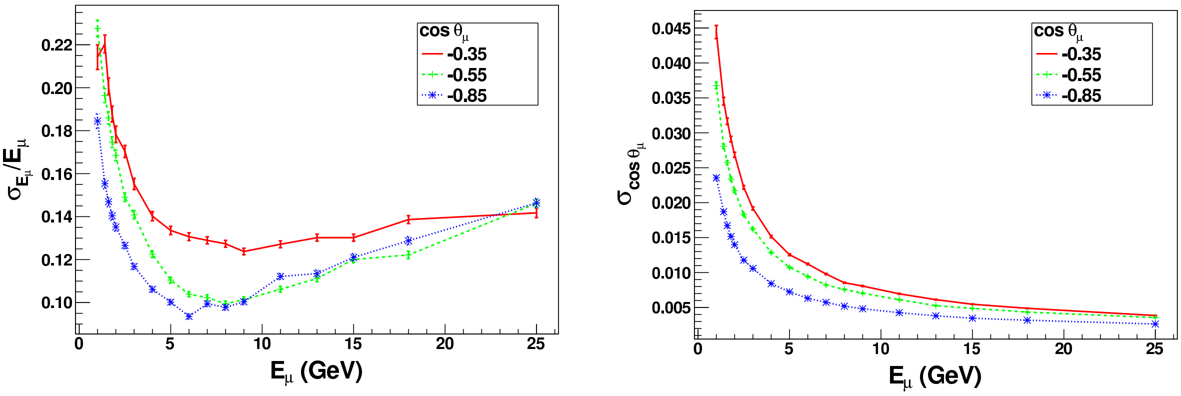

Figure 37: Muon energy (left) and zenith angle (right) resolutions [9].

then increases slightly. This is because at high energy, the muon track becomes too long leaving some energy outside the detector, hence larger energy uncertainty.

6.3.3 Improvement with Hadron Information

The muon energy is quite different from the neutrino energy. This is because the neutrino energy can deposit in both muon and the associated hadrons. Using only muon energy can lead to smearing effect from physical scattering process rather than detector response. To make the reconstruction of neutrino oscillation more precise, it is necessary to take both parts into consideration. For muon, this can be done quite precisely as discussed in Sec. 6.3.2 and particularly shown in Fig. 37. The difficult comes from the hadron part since most energy is absorbed in steal plates without being measured. From Fig. 38, we can observe that σ_E/E

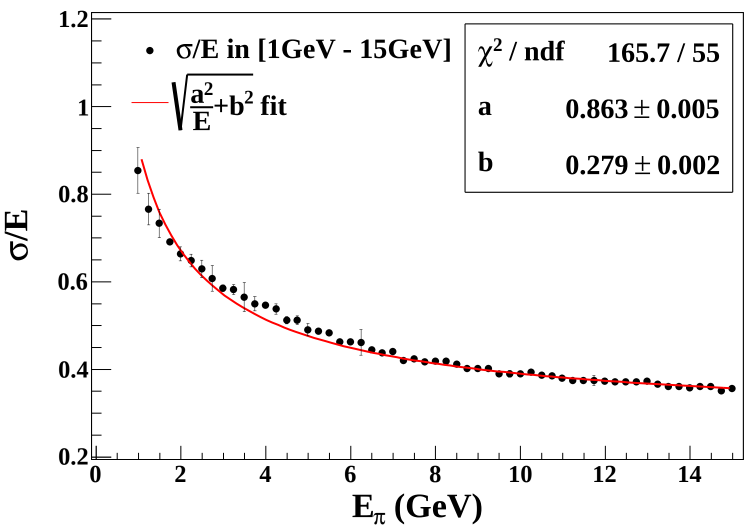

Figure 38: Hadron energy resolution [10].

is smaller at higher energy. This is because at lower energy, larger part of the hadron energy is absorbed in steal plates, making the relative difference between the measured and the true hadron energy have larger variation.

6.3.4 Neutrino Mass Hierarchy

According to Sec. 6.3.1, the MSW resonance can happen for neutrino or anti-neutrino, depending on the neutrino mass hierarchy, but not in both. This makes the difference between the neutrino and anti-neutrino oscillation probabilities to be maximal. The Fig. 39 shows the leading term of neutrino oscillation probabilities which are approximately,

$$P^{(0)}_{ee} \approx |S'_{11}|^2 \,, \qquad P^{(0)}_{e\mu} \approx P^{(0)}_{\mu e} \approx \frac{1}{2}\left(1 - |S'_{11}|^2\right) \,, \qquad P^{(0)}_{\mu\mu} \approx \frac{1}{4}\left|S'_{22} + S'_{33}\right|^2 \,, \tag{6.12}$$

where S' is the oscillation amplitude matrix in the propagation basis [11, 12]. We can see that around 5GeV

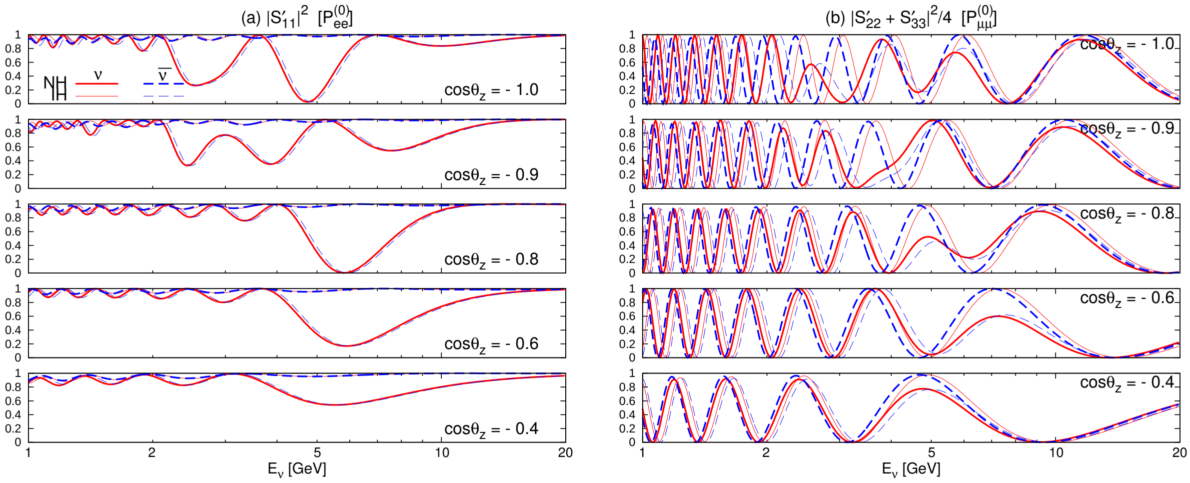

Figure 39: The atmospheric mixing angle θ_{23} and the CP phase δ independent part of the neutrino (red) and anti-neutrino (blue) oscillation probabilities for both normal (NH, thick) and inverted (IH, thin) mass hierarchies [2].

there is a resonance. This happens for all five cases of the neutrino zenith angle $\cos\theta_z = -1, -0.9, -0.8, -0.6, -0.4$. For those travelling across the core of the earth, namely $\cos\theta_z = -1$ and $\cos\theta_z = -0.9$, there is an extra resonance at lower energy. This is the so-called oscillation length resonance [13, 14, 15, 16, 17, 18]. The MSW resonance is resonance in the mixing angle and hence the oscillation probability while the oscillation length resonance happens in the oscillation phase. The first happens once the matter potential is around the resonance value. For the second, a periodic potential is necessary. For two-neutrino oscillation, the transition probability is roughly,

$$P_{\alpha\beta} = \sin^2 2\theta \sin^2\left(\frac{L\delta m^2}{4E}\right) \,. \tag{6.13}$$

No matter in the mixing angle or the oscillation phase it happens, the resonance can make itself explicit in the oscillation probability.

The magnetized experiment is designed to be most sensitive to the neutrino mass hierarchy [19, 20, 21, 9]. From Fig. 36 and Fig. 37, especially the charge identification efficiency ϵ_{CID} and the energy resolution σ_E, we can see that the best performance can be achieved around 5GeV. According to previous studies [19, 20, 9], after 10-year running, the hierarchy sensitivity can reach 3σ which is similar to our own simulation.

6.3.5 Octant of the Atmospheric Mixing Angle

The coefficients of the atmospheric mixing angle θ_{23} term, $x_a \equiv \cos 2\theta_{23}$, are of the same order as the leading term, according to the decomposition formalism [2, 22] in the propagation basis. Actually, they are approximately functions of $|S'_{11}|^2$,

$$P^{(1)}_{ee} \approx 0 \,, \qquad P^{(1)}_{e\mu} \approx P^{(1)}_{\mu e} \approx -P^{(1)}_{\mu\mu} \approx -\frac{1}{2}\left(1 - |S'_{11}|^2\right) \,. \tag{6.14}$$

The energy and zenith angle dependence of $|S'_{11}|^2$ is illustrated in Fig. 39. We can see that its variation is as large as 1. Consequently, the magnitude of $P^{(1)}_{e\mu}$, $P^{(1)}_{\mu e}$, and $P^{(1)}_{\mu\mu}$ varies between 0 and 1/2. This means that θ_{23} can have sizable effect on the neutrino oscillation probabilities, providing an opportunity of determining the octant of θ_{23} with atmospheric neutrino oscillations [20, 9, 2].

References

[1] A.M. Dziewonski and D.L. Anderson. *Phys.Earth Planet.Interiors*, 25:297–356, 1981.

[2] Shao-Feng Ge, Kaoru Hagiwara, and Carsten Rott. *JHEP*, 1406:150, 2014.

[3] G. Battistoni, A. Ferrari, T. Montaruli, and P.R. Sala. *Astropart.Phys.*, 23:526–534, 2005.

[4] Orlando L.G. Peres and A. Yu. Smirnov. *Phys.Rev.*, D79:113002, 2009.

[5] L. Wolfenstein. *Phys.Rev.*, D17:2369–2374, 1978.

[6] L. Wolfenstein. *Phys.Rev.*, D20:2634–2635, 1979.

[7] S.P. Mikheev and A. Yu. Smirnov. *Sov.J.Nucl.Phys.*, 42:913–917, 1985.

[8] S.P. Mikheev and A. Yu. Smirnov. *Sov.Phys.JETP*, 64:4–7, 1986.

[9] Tarak Thakore, Anushree Ghosh, Sandhya Choubey, and Amol Dighe. *JHEP*, 1305:058, 2013.

[10] Moon Moon Devi, Anushree Ghosh, Daljeet Kaur, Lakshmi S. Mohan, Sandhya Choubey, et al. *JINST*, 8:P11003, 2013.

[11] Evgeny K. Akhmedov, A. Dighe, P. Lipari, and A.Y. Smirnov. *Nucl.Phys.*, B542:3–30, 1999.

[12] Hidekazu Yokomakura, Keiichi Kimura, and Akira Takamura. *Phys.Lett.*, B544:286–294, 2002.

[13] Q.Y. Liu, M. Maris, and S.T. Petcov. *Phys.Rev.*, D56:5991–6002, 1997.

[14] M. Maris and S.T. Petcov. *Phys.Rev.*, D56:7444–7455, 1997.

[15] S.T. Petcov. *Phys.Lett.*, B434:321–332, 1998.

[16] M. Chizhov, M. Maris, and S.T. Petcov. 1998.

[17] M.V. Chizhov and S.T. Petcov. *Phys.Rev.Lett.*, 83:1096–1099, 1999.

[18] M.V. Chizhov and S.T. Petcov. *Phys.Rev.*, D63:073003, 2001.

[19] Mattias Blennow and Thomas Schwetz. *JHEP*, 1208:058, 2012.

[20] Abhijit Samanta. *Phys.Rev.*, D80:113003, 2009.

[21] Abhijit Samanta. *Phys.Rev.*, D81:037302, 2010.

[22] Shao-Feng Ge and Kaoru Hagiwara. *JHEP*, 1409:024, 2014.

7 Dark Matter

7.1 Neutrinos from dark matter annihilation in the halo

Neutrinos can be copiously produced via dark matter (DM) annihilation or decay in the Galactic DM halo. For annihilating DM, the resulting neutrino energy spectrum can be a delta function if neutrino is the direct final state of DM annihilation, i.e. $\chi\chi \to \nu\nu$; it can also be a continuous energy spectrum, if DM annihilates into standard model fermions which subsequently decay producing neutrinos. In this section, we will focus on the case where the neutrino spectrum is a delta function, since the mono-energetic neutrinos are readily distinguished from the background. The differential flux of the anti-electron-neutrino in the $\chi\chi \to \nu\nu$ case is given by (neglecting neutrino oscillations)

$$\frac{d\phi_{\bar{\nu}_e}(E_{\bar{\nu}_e} = m_\chi, \psi)}{d\Omega} = \frac{1}{2}\frac{\langle\sigma_{\chi\chi\to\nu\nu}v\rangle}{4\pi m_\chi^2}\frac{1}{3}\int_{\rm los} dx \rho_\chi^2(r(x,\psi)) \equiv \frac{\langle\sigma_{\chi\chi\to\nu\nu}v\rangle}{24\pi m_\chi^2}J(\psi), \tag{7.1}$$

where the factor (1/3) averages over the three flavors, the factor (1/2) pertains to identical DM particle, the integral is carried out along the line of sight (los), $\rho_\chi(m_\chi)$ is DM density (mass), ψ is the angle away from the galactic center (GC), Ω indicates the direction of DM annihilation, $r(x,\psi) = (x^2 + R_\odot^2 - 2xR_\odot\cos(\psi))^{1/2}$ is the distance to the GC, $R_\odot = 8.5$ kpc is the distance from the GC to the solar system, x is the distance between us and the location of DM annihilation. For analysis without directional information, one can obtain the total anti-electron-neutrino flux

$$\phi_{\bar{\nu}_e}(E_{\bar{\nu}_e} = m_\chi) = \frac{\langle\sigma_{\chi\chi\to\nu\nu}v\rangle}{24\pi m_\chi^2}\int d\Omega J(\psi) \equiv \frac{\langle\sigma_{\chi\chi\to\nu\nu}v\rangle}{6m_\chi^2}J_{\rm avg} \tag{7.2}$$

where $J_{\rm avg}$ is the averaged J factor over the whole sky, which has a rather weak dependence on the details of the dark matter density distribution in the halo, for some commonly used dark matter profiles: Navarro-Frenk-White (NFW) [4], Moore [5], and Kravtsov [6]. We take the value $J_{\rm avg}/(R_\odot\rho_\odot^2) = 5$ [3], assuming $\rho_\odot = 0.4$ GeV/cm^3. Thus the anti-electron-neutrino flux at $E_{\bar{\nu}_e} = m_\chi$, is given by

$$\phi_{\bar{\nu}_e}(E_{\bar{\nu}_e} = m_\chi) \simeq 1.1\times10^2\,{\rm cm^{-2}\,s^{-1}}\cdot\frac{\rm MeV^2}{m_\chi^2}\cdot\frac{\langle\sigma_{\chi\chi\to\nu\nu}v\rangle}{3\times10^{-26}\,{\rm cm^3\,s^{-1}}} \tag{7.3}$$

The monoenergetic feature of the neutrinos due to dark matter annihilation considered here, makes them quite easy to be detected over the continuous backgrounds. The number of events due to the anti-electron-neutrino are given by [7]

$$\mathcal{N} \simeq \sigma_{\rm det}\,\phi_{\bar{\nu}_e}\,N_{\rm target}\,t\,\epsilon \tag{7.4}$$

where the detection cross section $\sigma_{\rm det}$ needs to evaluated at $E_{\bar{\nu}_e} = m_\chi$ for dark matter annihilation, the total neutrino flux $\phi_{\bar{\nu}_e}$ is given in Eq. (7.3), $N_{\rm target}$ is the number of target particles in the detector, t is the total time-exposure, and ϵ is the detector efficiency.

The neutrino experiment at CJPL can search for neutrinos in the energy range $E \sim (1-100)$ MeV. The dominant backgrounds come from reactor neutrino, supernova relic neutrino, and atmospheric neutrinos in the energy range of interest. For simplicity, we only consider DM mass above ~ 10 MeV, to avoid the reactor neutrino background. Electron antineutrinos can be detected via the inverse beta decay process $\bar{\nu}_e + p \to e^+ + n$. The energy resolution can be estimated as $\delta E/E = 8\%$. The signal events due to DM in the energy bin around the DM mass with bin width equal to twice energy resolution is computed, which is then compared to the background events to derive the discovery limits. As shown in Fig. (40), one can probe the DM annihilation cross section to $\sim 10^{-24}$ (10^{-25}) cm^3/s with 10 (100) kton-year exposure. Current exclusion limits on DM annihilation into neutrinos are given by KamLAND [1] and Super-Kamiokande [2].

7.2 Neutrinos from dark matter annihilation in the Sun

Another promising signal for indirect detection of dark matter is to look for energetic neutrinos from annihilation of dark matter that have accumulated in the Sun and/or Earth (for early discussions, see e.g. [8] [9] [10] [11] [12]). When the solar system moves through the dark matter halo, a dark matter particle can

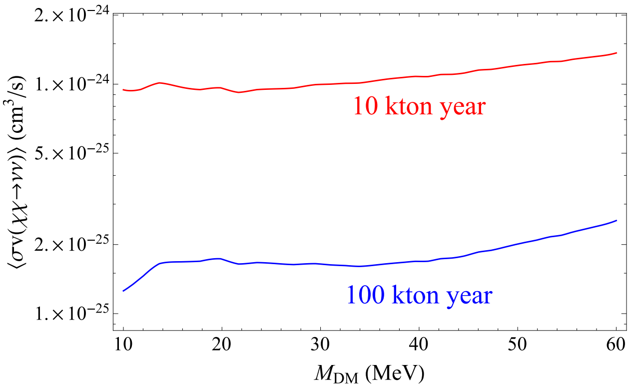

Figure 40: The discovery reach of the DM annihilation cross section for MeV mass range. The limits is derived with criteria $S = 5\sqrt{B}$ or 10 events, whichever is larger. Three backgrounds: supernova relic neutrino, atmospheric neutrino (both CC and NC) are considered. We assume 100% detection efficiency here.

scatter off a nucleus in the Sun or Earth and lose its velocity to be lower than the escape velocity, and thus becomes gravitationally trapped. The dark matter particle undergoes various scatterings in the Sun and eventually settles to the core, after the capture. Over the lifetime of the Sun, a sufficient amount of dark matter can accumulate in the core, so the equilibrium between capture and annihilation (or evaporation) is expected. Unlike other standard model particles, the neutrinos produced via dark matter annihilation can escape easily from the Sun and can be detected in neutrino experiments on Earth. The number of dark matter inside the Sun, N_χ, is described by the differential equation

$$\frac{dN_\chi}{dt} = C_C - C_A N_\chi^2 - C_E N_\chi \tag{7.5}$$

where the three constants describe capture (C_C), annihilation (C_A), and evaporation (C_E). For dark matter greater than the evaporation mass (which is typically 3-4 GeV [13] [14]), the C_E term can be ignored. The dark matter annihilation rate is given by [15]

$$\Gamma_A \equiv \frac{1}{2C_A N_\chi^2} = \frac{1}{2} C_C \tanh^2(t/\tau) \tag{7.6}$$

where $\tau \equiv 1/\sqrt{C_C C_A}$. The present dark matter annihilation rate is found for $t = t^\odot \simeq 4.5 \times 10^9$ years. When $t^\odot \gg \tau$, annihilation and capture are in equilibrium, so one has $\Gamma_A = C_C/2$. Thus, in equilibrium, the Γ_A only depends on the capture rate. Therefore, the resulting neutrino flux depends on the dark matter-nucleus cross section in the capture process, not on the annihilation cross section. The dark matter spin-dependent cross section, σ^{SD}, can be written as [15] [19]

$$\sigma^{\mathrm{SD}} = \kappa_f^{\mathrm{SD}}(m_\chi)\phi_\mu^f \tag{7.7}$$

where $\kappa_f^{\mathrm{SD}}(m_\chi)$ is the conversion factor between the spin-dependent cross section and the muon flux. The $\kappa_f^{\mathrm{SD}}(m_\chi)$ can be obtained from Figure 3 of ref. [15] for standard model final states, $f = W^+W^-, \tau^+\tau^-, t\bar{t}, b\bar{b}$, from which the neutrinos come from. These curves are based on calculations using DarkSUSY [20]. Super-Kamiokande [16] experiment has the best constraint on dark matter spin-dependent cross section from neutrino telescope experiments.

Search for neutrinos from dark matter annihilation in the Sun is totally possible as those from the halo. More studies are in progress on the sensitivity of Jinping experiment.

References

[1] A. Gando *et al.* [The KamLAND Collaboration], Astrophys. J. **745**, 193 (2012) [arXiv:1105.3516 [astro-ph.HE]].

[2] S. Palomares-Ruiz and S. Pascoli, Phys. Rev. D **77**, 025025 (2008) [arXiv:0710.5420 [astro-ph]].

[3] H. Yuksel, S. Horiuchi, J. F. Beacom and S. Ando, Phys. Rev. D **76**, 123506 (2007) [arXiv:0707.0196 [astro-ph]].

[4] J. F. Navarro, C. S. Frenk and S. D. M. White, Astrophys. J. **462**, 563 (1996) [astro-ph/9508025].

[5] B. Moore, T. R. Quinn, F. Governato, J. Stadel and G. Lake, Mon. Not. Roy. Astron. Soc. **310**, 1147 (1999) [astro-ph/9903164].

[6] A. V. Kravtsov, A. A. Klypin, J. S. Bullock and J. R. Primack, Astrophys. J. **502**, 48 (1998) [astro-ph/9708176].

[7] M. Wurm *et al.* [LENA Collaboration], Astropart. Phys. **35**, 685 (2012) [arXiv:1104.5620 [astro-ph.IM]].

[8] J. Silk, K. A. Olive and M. Srednicki, Phys. Rev. Lett. **55**, 257 (1985).

[9] L. M. Krauss, K. Freese, W. Press and D. Spergel, Astrophys. J. **299**, 1001 (1985).

[10] K. Freese, Phys. Lett. B **167**, 295 (1986).

[11] L. M. Krauss, M. Srednicki and F. Wilczek, Phys. Rev. D **33**, 2079 (1986).

[12] T. K. Gaisser, G. Steigman and S. Tilav, Phys. Rev. D **34**, 2206 (1986).

[13] K. Griest and D. Seckel, Nucl. Phys. B **283**, 681 (1987) [Erratum-ibid. B **296**, 1034 (1988)].

[14] A. Gould, Astrophys. J. **321**, 560 (1987).

[15] G. Wikstrom and J. Edsjo, JCAP **0904**, 009 (2009) [arXiv:0903.2986 [astro-ph.CO]].

[16] K. Choi *et al.* [Super-Kamiokande Collaboration], Phys. Rev. Lett. **114**, no. 14, 141301 (2015) [arXiv:1503.04858 [hep-ex]].

[17] M. G. Aartsen *et al.* [IceCube Collaboration], Phys. Rev. Lett. **110**, no. 13, 131302 (2013) [arXiv:1212.4097 [astro-ph.HE]].

[18] M. M. Boliev, S. V. Demidov, S. P. Mikheyev and O. V. Suvorova, JCAP **1309**, 019 (2013) [arXiv:1301.1138 [astro-ph.HE]].

[19] T. Tanaka *et al.* [Super-Kamiokande Collaboration], Astrophys. J. **742**, 78 (2011) [arXiv:1108.3384 [astro-ph.HE]].

[20] P. Gondolo, J. Edsjo, P. Ullio, L. Bergstrom, M. Schelke and E. A. Baltz, JCAP **0407**, 008 (2004) [astro-ph/0406204].